General Disclaimer

One or more of the Following Statements may affect this Document

- This document has been reproduced from the best copy furnished by the organizational source. It is being released in the interest of making available as much information as possible.

- This document may contain data, which exceeds the sheet parameters. It was furnished in this condition by the organizational source and is the best copy available.

- This document may contain tone-on-tone or color graphs, charts and/or pictures, which have been reproduced in black and white.

- This document is paginated as submitted by the original source.

- Portions of this document are not fully legible due to the historical nature of some of the material. However, it is the best reproduction available from the original submission.

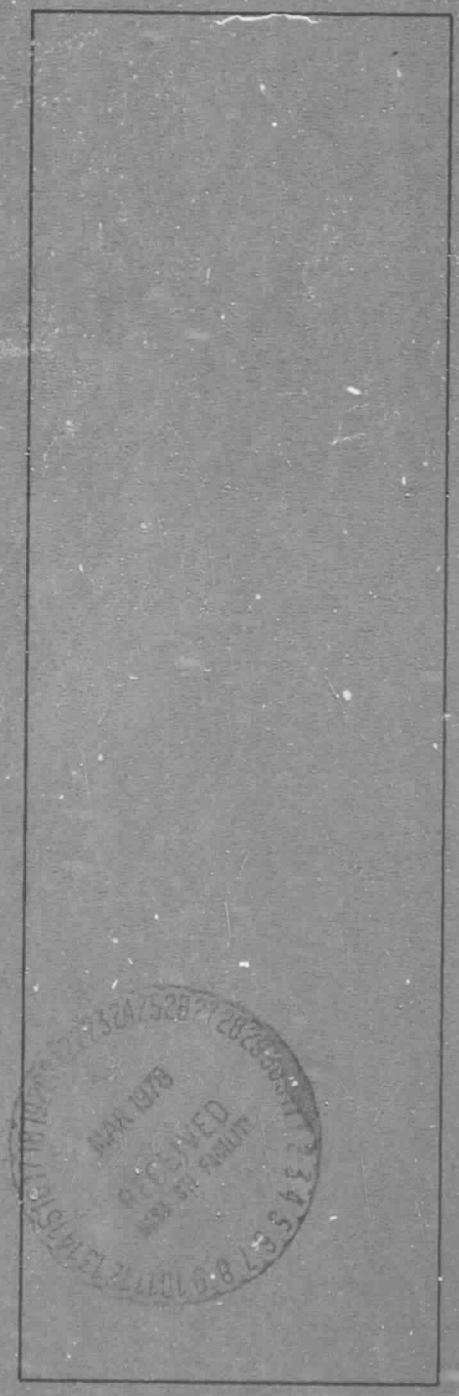

Bendix Guidance Systems Division

EXHIBIT B
FINAL REPORT

ALTERNATE BEARING DESIGN FABRICATION AND TEST PROGRAM

CONTRACT NO.
NAS-8-31236

20 FEBRUARY 1978

PREPARED FOR:

GEORGE C. MARSHALL
SPACE FLIGHT CENTER

MARSHALL SPACE FLT.
CENTER
HUNTSVILLE, ALABAMA
35812

PREPARED BY:

THE GYROSCOPIC
DEVICES LABORATORY
BENDIX CORPORATION
GUIDANCE SYSTEMS
DIVISION
TETERBORO, N. J.

/ss

TABLE OF CONTENTS

PREFACE

This report as submitted completes the requirements of Exhibit "B" of the Statement of Work for NASA Contract NAS-8-31236. The work performed herein is in accordance with the instructions of Supplemental Agreement Modification 2 dated 2 February 1976.

ACKNOWLEDGEMENT

An existing Bendix 50 ft-lb-sec Reation/Momentum Wheel, P/N 3980007-1, was modified by Bendix Guidance Systems Division, Teterboro, New Jersey to accept a magnetic bearing suspension. A new ironless stator, brushless DC motor and motor drive built by GSD was also installed. The magnetic suspension design was subcontracted to the Cambion Corporation, Cambridge, Massachusetts and was built and installed by Cambion.

The work has been carried out by the Gyroscopic Devices Laboratory of Bendix Guidance Systems Division under the cognizance of Paul Golley of the E&C Lab of Marshall Space Flight Center. R. Abramowitz, was the program manager. Technical coordination was performed by P. Makus, cognizant engineeer, assisted by H. Kalfaian, magnetic devices, and C. Gurrisi, mechanical development. The effort at Cambion Corporation was performed by P. Simpson, project engineer and A. Yamamura, senior design engineer with consultation by J. Lyman, research scientist.

ABSTRACT

An existing Bendix 50 ft-lb-sec Reaction Wheel was modified with an ironless armature brushless DC motor and a magnetic bearing suspension. The purpose of the enjoined task was to demonstrate the performance of an alternate bearing concept, i.e., a magnetic bearing suspension, which could be used in Skylab type CMG's to meet the attitude control equirements of future long term space stations. A magnetic suspension was built, installed and tested in the 50 FPS Reaction Wheel. A secondary effort included the build and test of a compatible reaction wheel motor. Performance characteristics of both are presented and discussed.

SECTION 1.0
INTRODUCTION

This program was initiated in response to a Marshall Space Flight Center RFP issued in November of 1975. The purpose of this effort was to demonstrate the performance of an alternate bearing concept to provide a very long life bearing to meet the requirements of future applications such as CMGs for a space station. Another requirement of this program was that the contractor demonstrate the alternate bearing design by adapting existing contractor owned hardware (CMG or Reaction Wheel) for the demonstration and that the bearing design be evaluated and compared to the performance of the previous (original) bearing design.

Bendix Guidance Systems Division's response to this RFP proposed to demonstrate the concept of a magnetic bearing for CMG's for very long life by modifying our existing 50 ft-lb-sec reaction wheel to accommodate a two axis active radial, one axis passive axial magnetic suspension system. We proposed that functional tests be performed to evaluate the magnetic bearing design and to allow comparisons to be made with the original reaction wheel in its standard ball bearing configuration. In addition to incorporating a Magnetic Suspension System GSD also proposed to install and test an ironless armature brushless DC spin motor in this unit.

Because of their previous experience in the field of magnetics the magnetic suspension portion of this effort was subcontracted to Cambridge Thermionic Corporation (Cambion) of Cambridge, Mass.

SECTION 2.0
SUMMARY

The Bendix 50 ft-lb-sec momentum/reaction wheel was modified to demonstrate the feasibility of a magnetic suspension for this size of reaction wheel. The wheel had a one piece spoked rotor weighing over 17 pounds. It was contained in a pancake style housing as shown in Figure 2-1. The original configuration incorporated an AC induction drive motor. This wheel was to be modified with a new ironless stator brushless DC motor, optical tachometer and radially active magnetic suspension bearing. The intent of this project was to only add the above components keeping all else the same. However, it became necessary to replace the spoked upper bearing support housing with a solid aluminum plate later in the program. This was done to relieve warping which disallowed operation of the magnetically suspended wheel in its own vacuum housing. Table 2-1 lists the predominant features of the 50 ft-lb-sec Magnetic Bearing Suspension Reaction Wheel (MBSRW).

The resultant MBSRW is shown with vacuum covers off in Figures 2-2 and 2-3. The solid upper bearing support plate is shown in Figure 2-2. It is of two piece construction to allow independent alignment of the upper and lower bearing support shown in Figure 2-3. The wheel housing outline has remained the same with the thickness growing only 1-1/8 inch to accommodate the added rate sensors. Weight efficiency was not a prime consideration for this project.

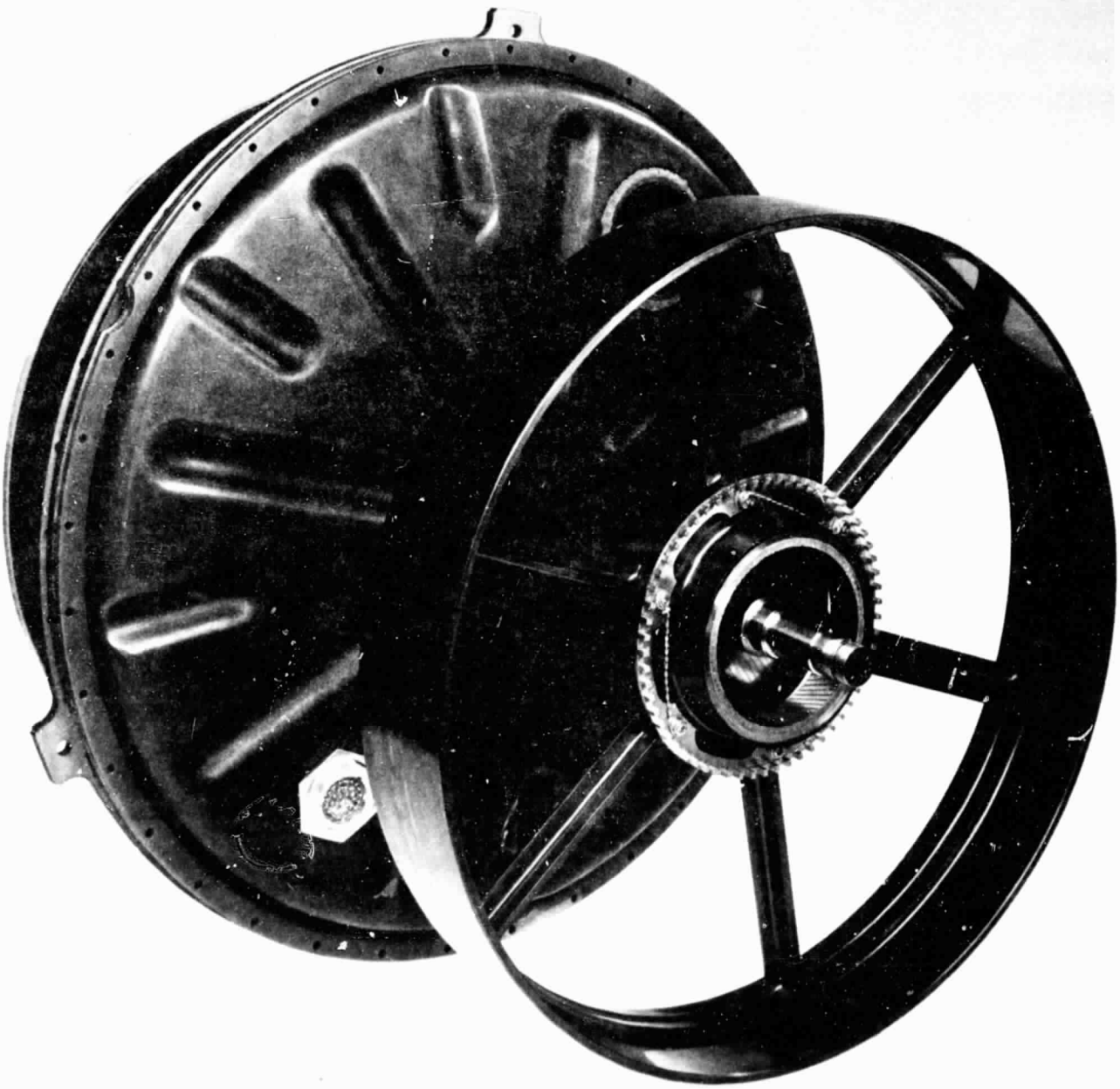

50 FT-LB-SEC MOMENTUM WHEEL

FIGURE 2-1

TABLE 2-1

50 FPS MAGNETIC BEARING SUSPENSION REACTION WHEEL

CONFIGURATION	SPOKED ONE PIECE ROTOR IN PANCAKE STYLE HOUSING
SIZE	18.75" DIA BY 8.5" (EXC MTG HOLES)
WEIGHT	
WHEEL ASSEMBLY (ORIGINAL CONFIG.)	32 LBS
NEW MAGNETIC SUSP. ASSY (EXC ELEC)	69 LBS
ANGULAR MOMENTUM	60 FT-LB-SEC AT 3000 RPM
MAXIMUM OUTPUT TORQUE	60 OZ-IN
WHEEL BEARING	TWO AXIS RADIALLY ACTIVE MAGNETIC SUSPENSION
TOUCHDOWN BEARINGS	ANGULAR CONTACT 104H BALL BEARINGS
WHEEL MOTOR	IRONLESS STATOR BRUSHLESS DC MOTOR
WHEEL SPEED INDICATION	TWO PHASE 60 PULSES PER REVOLUTION OPTICAL TACHOMETER

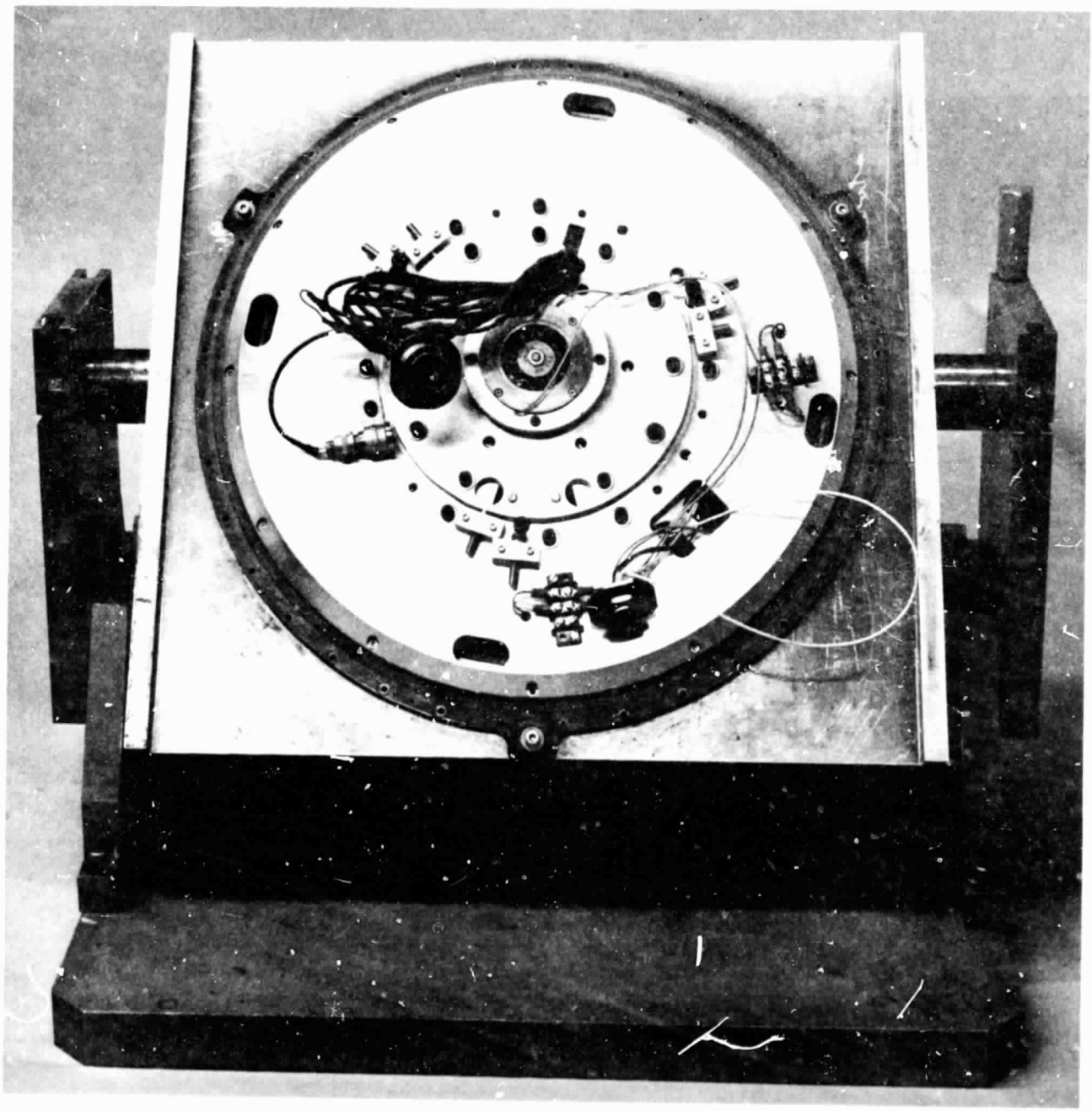

50 FPS MAGNETIC BEARING SUSPENSION REACTION WHEEL
(TOP VIEW)
FIGURE 2-2

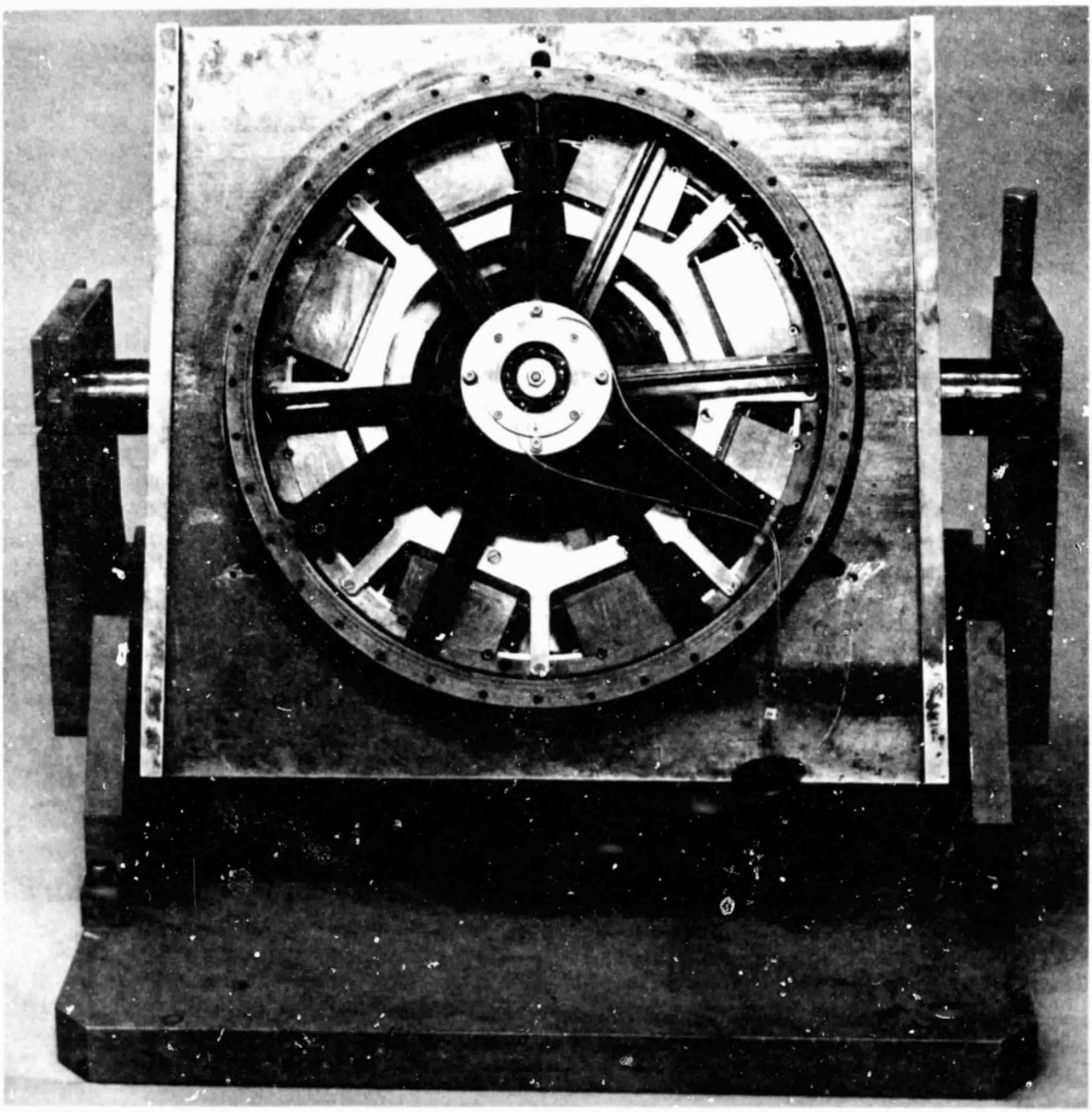

5' FPS MAGNETIC BEARING SUSPENSION REACTION WHEEL
(BOTTOM VIEW)
FIGURE 2-3

The magnetic suspension was built and installed by the Cambion Corporation, Cambridge, Massachusetts. The ground rules used in designing the magnetic suspension were that it had to be fitted to the existing 50 ft-lb-sec wheel and be contained within its envelope. This essentially dictated that a two axis radially active suspension at the rim be used. A continuous magnetic steel ring was shrunk fit into the rim as shown in Figure 2-4. This ring is magnetically attracted by the suspension stator in a radial direction. Force coils located along two orthogonal radial axes provide the necessary stabilization forces. The suspension is passive in the axial direction. The fringing rings shown act to increase the axial stiffness. The clear band between is the target surface for the capacitance displacement sensors.

The stationary portion of the magnetic suspension; magnets, magnetic steel and force coils are located in the magnetic suspension stator assembly as shown in Figure 2-5. The stator assembly consists of two continuous magnetic steel rings and eight suspension blocks. The stator rings have matching fringing rings as shown in Figure 2-6. The spacer between them is aluminum. The discrete suspension blocks contain the rare earth Samarium Cobalt magnets in series with the electrical force coils. Four suspension blocks are used for each orthogonal radial axis with the magnetic fields at the gap being smoothed by the continuous steel rings.

Stabilization is accomplished in the servo amplifiers

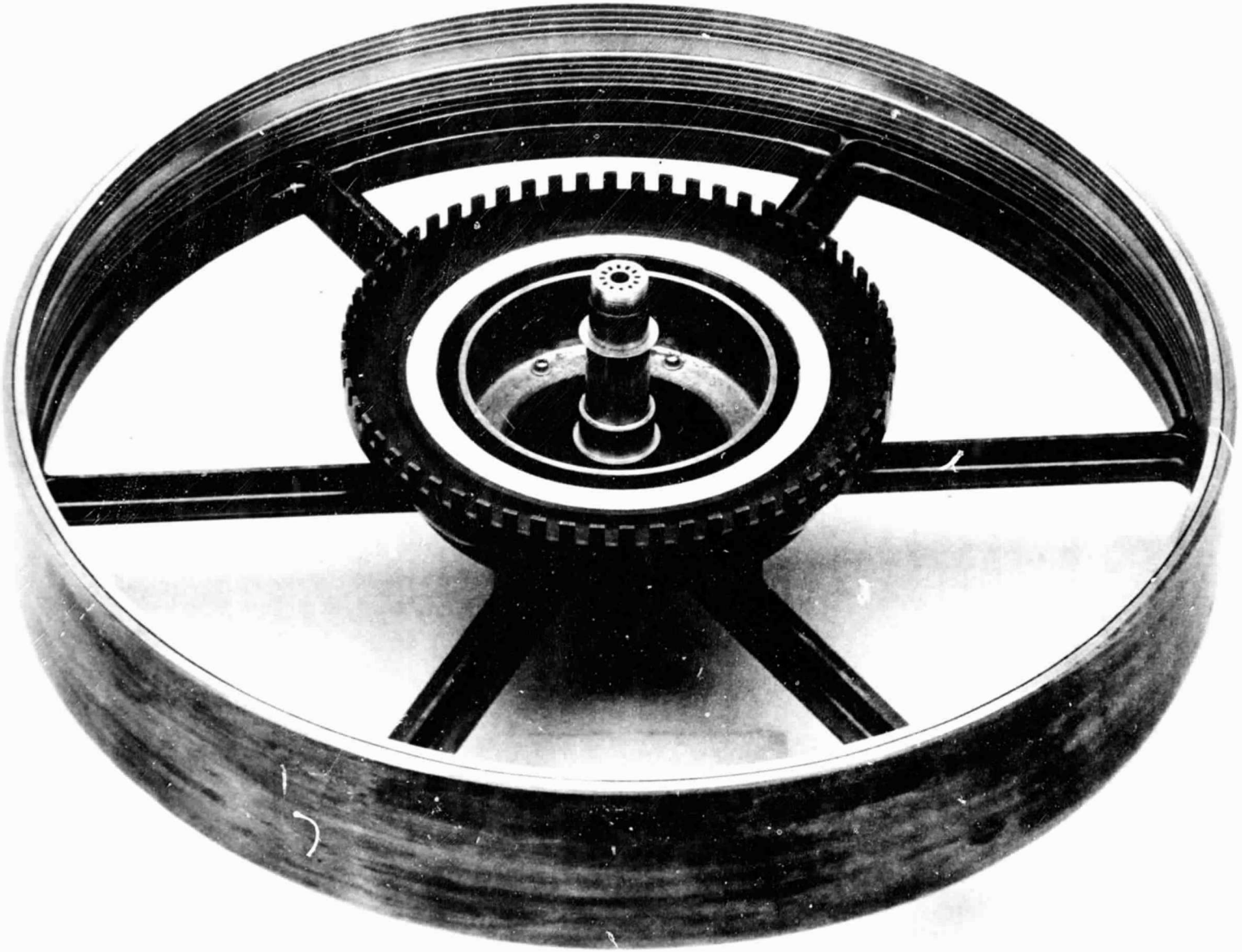

50 FPS WHEEL WITH SUSPENSION ROTOR INSTALLED

FIGURE 2-4

MAGNETIC SUSPENSION STATOR ASSEMBLY

FIGURE 2-5

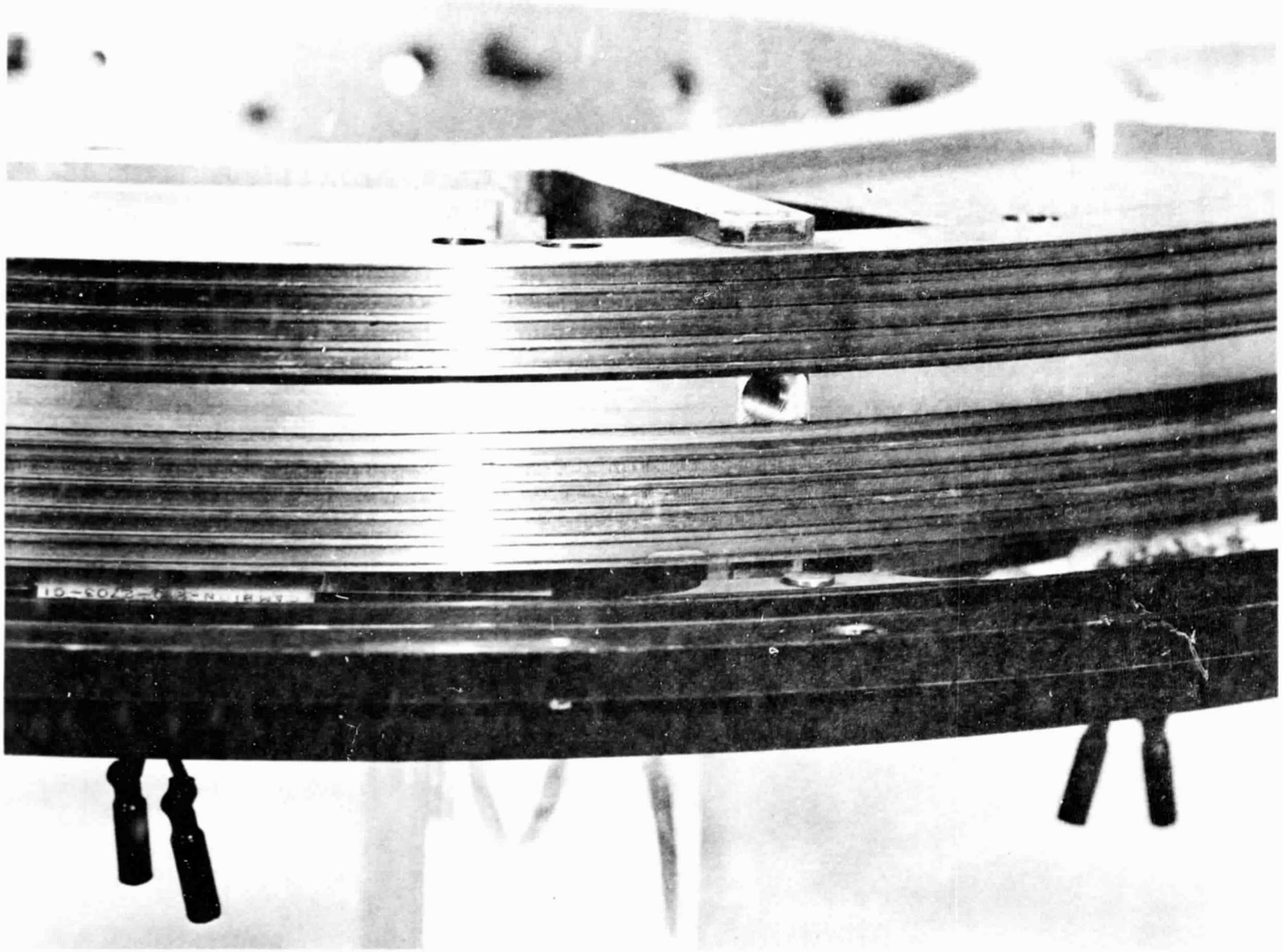

MAGNETIC SUSPENSION STATOR RINGS

FIGURE 2-6

using displacement and velocity sensors. Two capacitance sensors, one for each axis, are located in the magnetic gap at the wheel rim. Two two-axis Faraday velocity sensors are located at both ends of the rotor's shaft. Table 2-2 lists the characteristics of the 50 ft-lb-sec reaction wheel's magnetic suspension. The reaction wheel has been tested in vacuum with speeds up to 2000 rpm, however, resonances and vibrations have caused unsatisfactory operation above 1000 rpm at the present time.

Prior to the installation of the magnetic suspension, an ironless stator brushless DC motor was put into the reaction wheel. This motor was installed to eliminate radial motor forces from disturbing the magnetic suspension. Conventional brushless DC and AC induction motors have radial forces generated between the rotating iron and the stator iron. Figure 2-7 shows the ironless motor stator mounted on the upper bearing support assembly. The motor rotor consisting of Samarium cobalt magnets and magnetic return iron is shown in Figure 2-8. Performance characteristics of the motor are listed in Table 2-3. Although this motor does not have a magnetic drag per se, it unfortunately does have a drag caused by electrical braking due to uncancelled circulating currents in the motor windings.

The brushless DC motor is driven by a Pulse Width Modulated (PWM) current amplifier. The motor torque is linearly proportional to motor current and thus linearly

proportional to torque command voltages to the PWM. Hall elements imbedded in the motor stator provide the necessary commutation signals for the PWM. Power is applied to the motor windings through a pulse width modulated H-bridge. Table 2-4 lists the characteristics of the subsystem of PWM, motor and wheel. The PWM is shown in Figure 2-9.

TABLE 2-2

50 FPS MAGNETIC SUSPENSION CHARACTERISTICS

SUSPENSION TYPE	TWO AXIS, RADIALLY ACTIVE, AXIALLY PASSIVE
LOCATION	MAGNETIC BEARING MOUNTED INSIDE RIM OF THE WHEEL
MAGNET MATERIAL	SAMARIUM COBALT
SENSORS	
DISPLACEMENT	CAPACITANCE
VELOCITY	FARADAY
RADIAL STIFFNESS	10,000 LBS/INCH
MAXIMUM EXCURSION	$\pm$0.0075 INCH
SUPPORT CAPABILITY	$\pm$75 LBS
AXIAL STIFFNESS	4,500 LBS/INCH
MAX EXCURSION	$\pm$0.030 INCH
SUPPORT CAPABILITY	$\pm$135 LBS
MAGNETIC DRAG	1.9 OZ-IN AT 1000 RPM
POWER REQUIREMENTS	
PEAK (LIFTOFF)	150 WATTS
STEADY STATE	1.4 WATTS
OPERATING BUSS	28 VDC $\pm$ 4V
SUSPENSION WEIGHT	
ROTATING	2 LBS
NON-ROTATING (EXC ELECT)	35 LBS

IRONLESS BRUSHLESS DC MOTOR STATOR ASSEMBLY

FIGURE 2-7

IRONLESS STATOR, BRUSHLESS DC MOTOR ROTOR ASSEMBLY
FIGURE 2-8

TABLE 2-3

50 FPS BRUSHLESS DC MOTOR CHACTERISTICS

MOTOR TYPE	ROTOR OUTSIDE STATOR, BRUSHLESS DC IRONLESS STATOR
COMMUTATION	HALL ELEMENTS ON STATOR
NO. POLES	12
NO. PHASES	2
SIZE	5.50" OD X 3.95" ID X 1.80" LENGTH
WEIGHT	38 OUNCES
MAGNET MATERIAL	SAMARIUM COBALT
MAXIMUM TORQUE	60 OZ-IN
TORQUE SCALE FACTOR	8.35 OZ-IN/P K AMP
MAXIMUM SPEED	3000 RPM
PEAK POWER AT 2500 RPM AND MAX TORQUE	130 WATTS
MOTOR CONSTANT (MAX)	11-18 OZ-IN/ WATT*
BACK EMF CONSTANT	0.00618 VOLTS PK/RPM
MOTOR TIME CONSTANT	0.2 MILLISECONDS
DC RESISTANCE (EACH PHASE)	0.22 OHMS
TOTAL AC IMPEDANCE (EACH PHASE)	0.49 OHMS
INDUCTANCE (EACH PHASE)	0.05 MILLIHENRIES
DRAG TORQUE NEAR ZERO SPEED	
(BALL BEARING)	0.4
(CIRCULATING MOTOR CURRENT)	0.1
DRAG TORQUE AT 3000 RPM	
(BALL BEARING)	1.5
(CIRCULATING MOTOR CURRENT)	2.8 OZ-IN
EFFICIENCY AT 2500 RPM	
(MAX TORQUE)	82%
(20% TORQUE)	93%

*UNCERTAINTY DUE TO VERY LOW MOTOR RESISTANCE

TABLE 2-4

MOTOR DRIVE CHARACTERISTICS

INPUT POWER	28 ± 4 VDC
TORQUE COMMAND SIGNAL	0 to ±5 VDC
TORQUE COMMAND SCALE FACTOR	11.7 OZ-IN/VOLT
	8.35 OZ-IN/PK AMP
PEAK POWER AT 2500 RPM AND MAX TORQUE	208 WATTS
QUIESCENT POWER AT ZERO SPEED	8.5 WATTS
EFFICIENCY AT 2500 RPM (MAX)	59%
(MIN)	52%
PWM FREQUENCY	9.6 KHZ
TYPE	BRASSBOARD

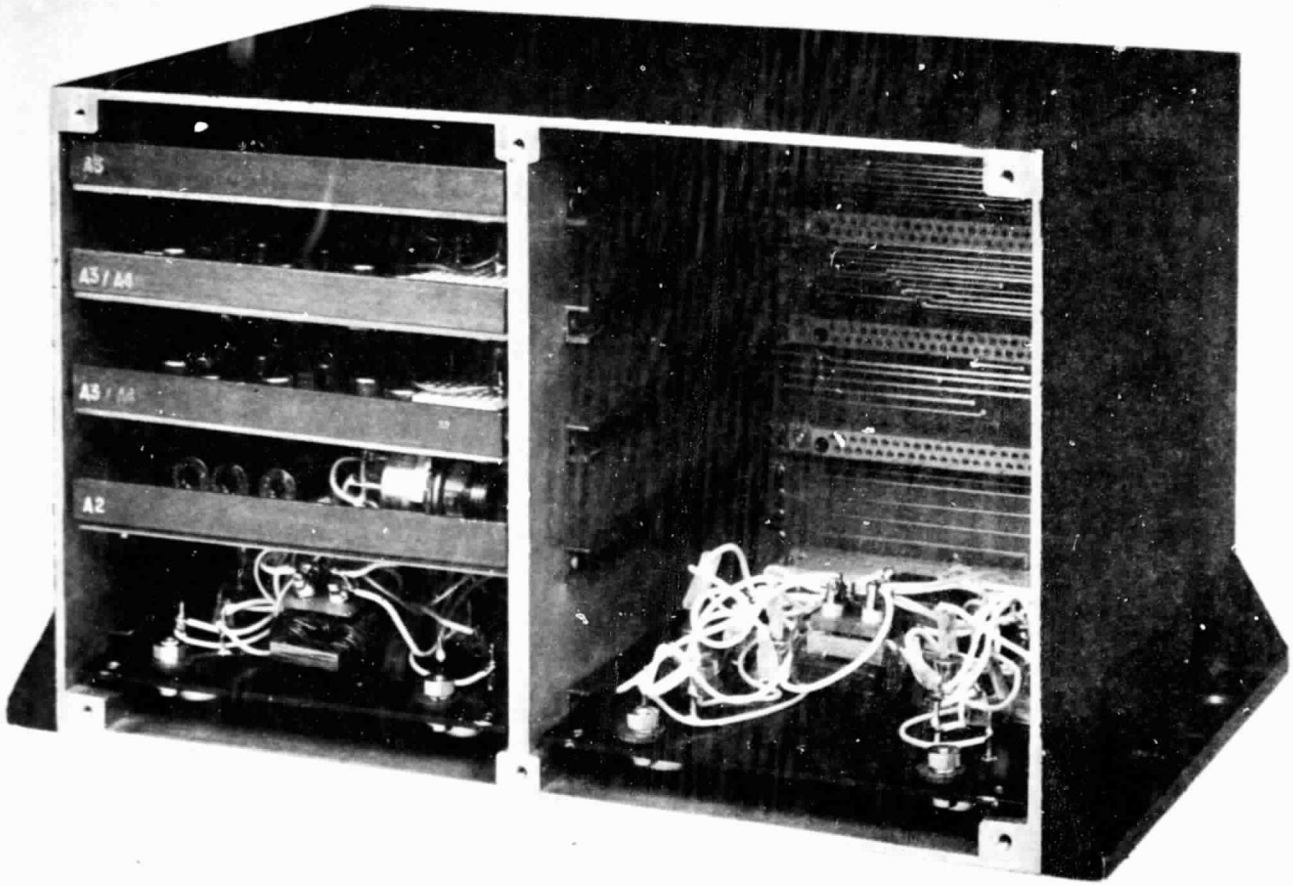

BRUSHLESS DC MOTOR PWM DRIVE ELECTRONICS

FIGURE 2-9

SECTION 3.0
REACTION WHEEL DESIGN

3.1 EXISTING CONFIGURATION

The Bendix Corporation, Guidance Systems Division, has fabricated and functionally tested a 50 ft-lb-sec Momentum Wheel. This unit was designed such that it could be operated as a reaction wheel (thru zero speed operation), a biased momentum wheel (constant speed operation), a reaction wheel scanner and finally as a wheeled section of a low output torque control moment gyro, either single or dual gimballed.

The unit consists of a six (6) spoke 16 inch diameter wheel in a magnesium housing. This unit develops 50 ft-lb-sec of angular momentum at a flywheel speed of 3000 RPM. The completed unit is 16.5 inches in diameter and 7.25 inches high. The magnesium housing has three bosses on a 19 3/16 inch diameter bolt circle providing a three-point mount for the unit. The total unit weight is 32 pounds.

In design and fabrication of this unit we combined our reaction wheel housing and wheel technology with our CMG bearing support system.

The unit's housing consists of a cylindrical shell with a three-spoked truss structure extending from both sides of the shell to support the bearing cartridges. This type of support structure reduces the overall unit weight, without sacrificing the necessary rigidity required by

the rotating mass. In order to maintain a low pressure or vacuum environment within the housing to minimize windage drag torques, two hydro-formed aluminum covers, separate from the three spoked support are provided. Both covers use a modular molded viton seal which allows for easy assembly and disassembly. Because the external covers and spoked support truss are separate members, the unit's bearing and preload arrangement are insensitive to pressure differentials between the unit's cavity environment and the external environment. In order to limit vibration input to the spin bearings, excursion limiters (bumper stops) were machined as part of the external cylindrical housing. Whenever the vibration loads become excessive, impact between the bumper stops and the flywheel rim face would shunt the load to the spin bearings, thus protecting the bearings from damage during any vibration exposures.

The flywheel for this momentum wheel was machined from a single billet of high strength steel. This included the bearing journals, the motor rotor hub, the spokes, and the wheel rim. This single piece construction was chosen to assure balance stability and bearing alignment. The spin motor rotor and its hub is secured to the flywheel by bolting the hub to threaded bosses on the flywheel spokes within a pilot diameter.

The flywheel is supported within the structure by single 104H angular contact ball bearings. A 10 pound axial preload is provided by belleville springs. The bearings contain modified phenolic retainers specially machined for stable performance, low drag torque, and the acceptance of a continuous supply of lubricant from a dynamic lubrication system. Oil is metered to the bearing retainer at an approximate flow rate of 0.01 mg/hr from the dynamic lubrication system which operates on centrifugal pressure. This lubrication system is similar to that developed by BNC for Skylab CMG's. Bendix CMG's have a massed in excess of 400,000 operating hours on this type of bearing and lubrication system with no failures. Ten of these have each accumulated over 20,000 hours of run time.

The bearing support system includes a steel slider shrunk fitted to beryllium cartridges attached to the three-spoke truss members. By utilizing steel slider - cartridge assembly, and belleville spring preload on both spin bearings, the unit is able to tolerate coefficient of expansion mismatches between the housing and flywheel material. The beryllium bearing support housing was utilized to provide improved heat transfer to the housing.

This momentum wheel was instrumented with a magnetic speed pick-up and 60 tooth speed gear to monitor wheel speed. A thermistor, is used in the proximity of one bearing to monitor bearing temperature. A thermopile

vacuum sensor is used to monitor cavity pressure and a quartz crystal accelerometer to measure wheel unbalance and monitor bearing condition.

The current unit as previously described was initially assembled with a two phase AC induction spin motor developing 14 oz-in of torque at stall and 10 oz-in of reaction torque between 1800 and 2400 RPM. The second time this unit was assembled, motive power was supplied by a two phase brushless DC spin motor capable of supplying $\pm$20 oz-in of reaction torque across a speed range of $\pm$3000 RPM. Finally the unit was assembled with an ironless stator brushless DC spin motor. This experimental motor delivered a peak torque of 60 oz-in.

3.2 MODIFIED CONFIGURATION FOR MAGNETIC BEARING

The existing 50 ft-lb-sec momentum wheel was structurally modified to accept the necessary hardware to magnetically suspend the unit's flywheel. The flywheel, support structure, and bearing configuration were modified to incorporate the magnetic suspension, and provide mechanical touchdown bearings.

The six spoke high strength steel flywheel was fitted with the magnetic suspension rotor pole ring fabricated from AISI C1018 steel. This rotor pole ring was shrunk fit to the inside diameter (14.935 inches) of the flywheel rim. Final machining of the rotor pole ring to obtain the fringing ring configuration was performed on this subassembly level to maintain accurate concentricties of the rings to the flywheel's spin axis.

A twelve pole motor rotor and rotor support hub integral with a sixty tooth tach ring was assembled to the webbed section of the flywheel. This twelve pole rotor was designed for use with an ironless armature brushless DC motor. The sixty tooth tach pattern on the rotor support hub is compatible with a photo sensitive pickoff. The photo sensitive speed pickoff consists of two light emitting diodes and two photo transistors which are used to monitor the flywheel's speed and direction of rotation.

For increased stiffness the removable (top) three-spoke magnesium truss member that supported the bearing cartridges and motor stator was replaced with a solid disk of aluminum approximately one half inch thick. The increased stiffness of this member became a necessity because the stator mounting ring, (including magnetic suspension stator, motor stator, touchdown bearing cartridges and sensing devices), were all assembled to this main support. This main support was also stiffened to reduce resonant frequencies in the magnetic suspension.

The 104H angular contact ball bearings were further modified to be utilized as backup and touchdown bearings for the magnetic bearing. These bearings would provide support for the rotating mass in the event the magnetic suspension should malfunction, thus eliminating any damage to magnetic suspension hardware. Their secondary use is to support the flywheel during storage and shipment, so that no contact would be incurred between the suspension air gaps. The inner races of these bearings were ground oversize to provide a .007 inch radial gap

between the bearing inner race and flywheel shaft. The bearing outer races were locked to the bearing support cartridges and the flywheel was shimmed to provide a .030 inch axial gap between the flywheel shaft shoulder and inner race face. To prevent rotation between the bearing inner and outer races during operation of the magnetically suspended flywheel these bearings were lubricated with Andox "C" grease. This grease also provides adequate lubrication for the bearing in the event the rotating mass had to be supported by these bearings.

SECTION 4.0
MAGNETIC SUSPENSION DESIGN

The start of the magnetic suspension design began with the premise that an existing reaction wheel be used as the subject and that the suspension, less electronics, be wholly contained within the existing reaction wheel envelope. The intent of this approach was to show the feasibility of magnetically supporting a reaction wheel in the 50 ft-lb-sec to 100 ft-lb-sec class with a minimum of hardware development and growth in size. The use of the existing Bendix 50 ft-lb-sec wheel for this experiment predicated the design of a rim mounted suspension. Axial mounted suspensions would have violated the original premise since this wheel has a pancake style housing with no room for attaching an axial suspension. Rim suspensions can assume several configurations requiring a minimum of two controlled or servoed axes. The configuration chosen for this project was predicated on the geometry of the reaction wheel and the desire to minimize drawbacks normally associated with rim suspensions.

The foremost problems with rim suspensions are machining, weight and drag losses. Since the suspension requires magnetic steel paths of certain cross-sectional areas for its magnetic circuits, and since the magnetic gap is located at a nominal 16 inch diameter, the weight of the suspension grows rather rapidly. However, the suspension weight for this experiment was elected to be a minor consideration. A more serious problem arises in the form

of magnetic drag. Because of high magnetic flux densities and multiple servoed axes there will be flux variations in the air gap creating eddy currents and hence magnetic drag torques. Therefore, the suspension must be designed to have the flux in the air gap as uniform as possible. In this regard machining of the components also becomes critical since any variations will cause drag torques. The difficulty arises in attempting to machine parts to tolerances less than a thousandth of an inch at a 16 inch diameter. Even after assembly dimensional problems still exist due to forces of thousands of pounds per inch in the air gap tending to bend and distort the suspension. High bearing stiffnesses are required not only to support the 19 pound rotor weight but also to allow operation within the 3,000 RPM wheel speed range. Since the suspension will have at least one passive axis to reduce servo-mechanism complexity, the bearing stiffness for this axis, essentially undamped, must be greater than 5,000 pounds per inch to avoid wheel excited oscillations.

With the above considerations in mind, an attractive, two axis radially active, axially passive magnetic suspension was chosen. The operation of the suspension is shown schematically in Figure 4-1. Because of magnetic attraction the rotor will seek to maximize the magnetic force by minimizing the air gap. In the side view shown it is obvious that this will result in axial stability since the rotor rings will tend to align with the stator rings for minimum gap. It is also obvious that the system is

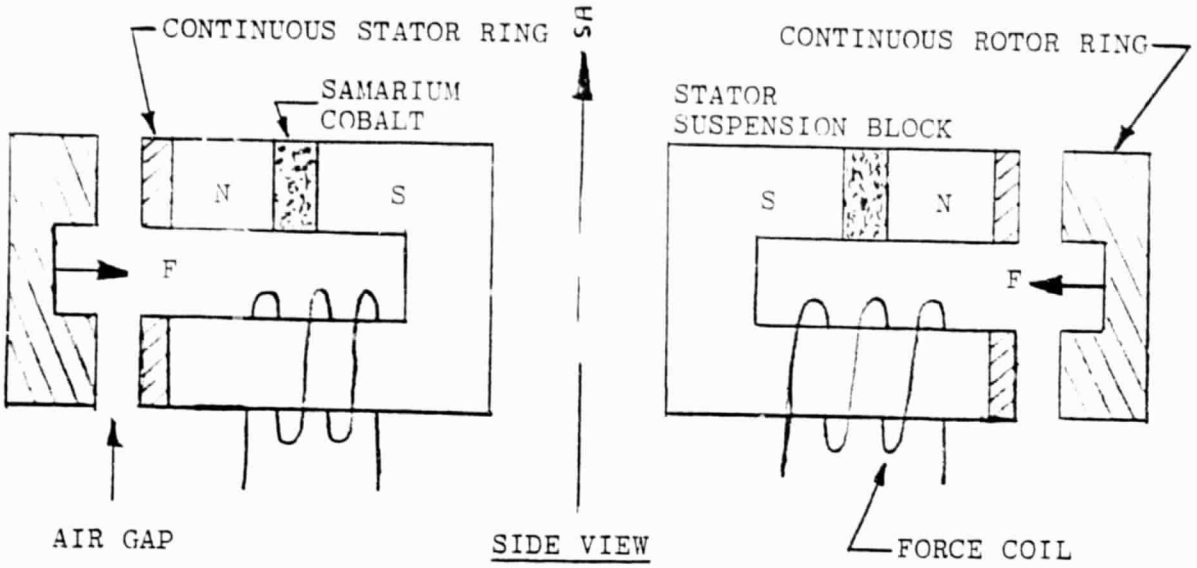

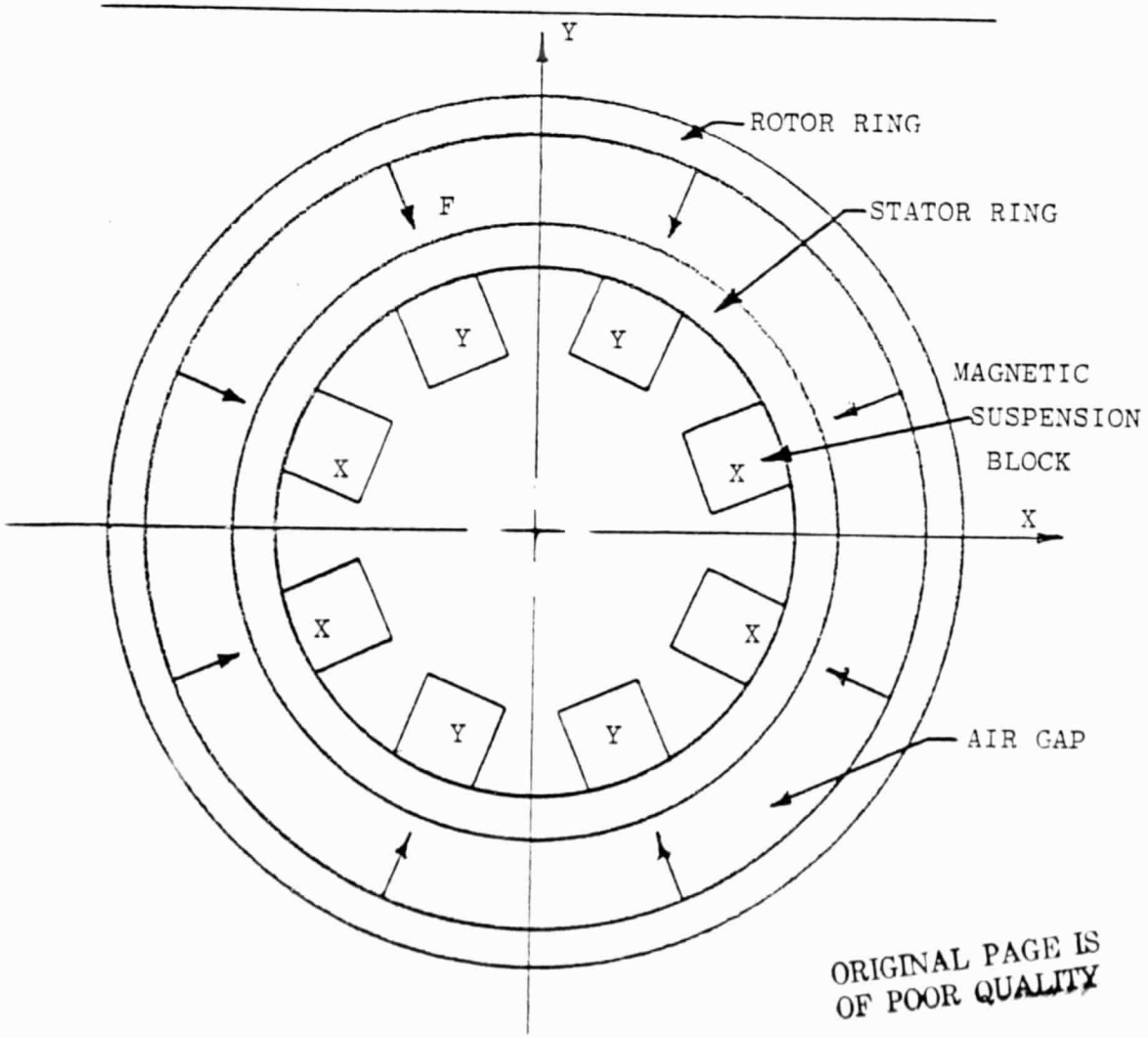

ORIGINAL PAGE IS OF POOR QUALITY

TOP VIEW

FIGURE 4-1

unstable radially since an imbalance between the two opposing radial forces will cause the stronger force to close the gap overcoming the weaker force thus causing touchdown. This radial action can be viewed as a negative spring since a deflection from nominal causes a negative force to be generated by the suspension to deflect even more therefore being inherently unstable. For this reason an electromagnetic force coil is connected in series with the permanent magnet flux to modulate the magnet forces in response to radial disturbances thus stabilizing the suspension. Displacement and velocity sensors complete the servo loop with the force coils in a servo amplifier.

The top view in Figure 4-1 shows how the eight discrete suspension blocks containing Samarium Cobalt magnets and force coils are arranged to provide the two active radial axes. Four suspension blocks are connected so that their vectored sum is orthogonal to the remaining four blocks. Therefore, the electromagnetic forces are summed vectorially along two orthogonal axes whereas the passive magnetic forces are distributed evenly around the circumference.

The rotor and stator rings which complete the magnetic flux circuit are continuous thus providing smoothing of the magnetic flux.

4.1 DEVELOPMENT HISTORY

Build of the magnetic suspension for the reaction wheel

began after the design was verified with a test fixture. The test fixture, consisting of one suspension block and a linear segment of the rotor and stator rings, was used to determine the magnetic bearing parameters. The fixture is discussed in the next section. The rotor ring was shrunk fit to the reaction wheel rotor and the fringing rings machined in the assembly. The stator rings were then manufactured along with the suspension blocks. The original air gap was supposed to have been 0.015 inch but when assembled was reduced to 0.013 inch by the magnetic forces. The magnetic forces were much stronger than anticipated and the gap was opened to 0.024 inch.

One of the problems encountered at this time was with the eddy current displacement sensors. During assembly and testing many sensors were broken due to the location of the sensors and the large forces created by the suspension. To alleviate this problem, a separate test fixture was made to hold only the wheel rotor and suspension stator assembly. The eddy current sensors were located external to the assembly on the wheel rim thus preventing breakage and allowing for observation. Figure 4-2 shows this test fixture in which the wheel was first suspended.

The suspension was to originally have been stabilized using derived rate signals from the displacement signals. During testing, however, it became apparent that more lead compensation than anticipated was needed for the force coils. Due to the structural resonances and other problems, the displacement signal was too noisy to be used for stabilization alone and Faraday rate generators

50 FPS MBSRW TEST FIXTURE

FIGURE 4-2

were required to provide the necessary lead compensation. The velocity sensors were attached to the rotor shaft in the space normally occupied by the ball bearing lubricating nut.

One of the troublesome problem areas during this time was touchdown bearing alignment. The wheel rotor was, of course, self aligning within the 0.024 inch magnetic gap, however, the ball bearings, having only a 0.007 inch gap, had to be aligned to the magnetic center. The wheel housing assembly was originally designed for ball bearings and although sufficient for their use proved inadequate for the magnetic suspension. Distortions of the housing assembly caused by magnetic forces made alignment of the touchdown bearings a tedious and difficult procedure.

Once the assembly was aligned attempts were made to operate the wheel in a vacuum environment. The units vacuum covers were put on and the unit evacuated. The housing, under vacuum pressure, would again distort causing touchdown of the magnetic suspension. This problem was particularly vexing since alignment was not returned upon release of the vacuum. It was at this point that it was decided to replace the upper bearing support housing with a more rigid structure which could be easily aligned.

The upper bearing support was replaced with two flat circular aluminum plates. The magnetic suspension was attached to the outer ring and has means of aligning the magnetic suspension to the lower touchdown bearing.

The inner ring holds the motor and upper touchdown bearing also with means of aligning to the suspension. This modification proved successful in allowing and maintaining alignment for the remainder of suspension tests which were performed including vacuum testing.

During this final phase of testing, a notch filter was added to the servo loop to eliminate a severe mechanical resonance in the reaction wheel. The wheel now ran smoothly up to 1000 rpm. At this speed surface irregularities due to the method of machining appeared to cause the suspension to go unstable. These irregularities were noticeable in the sensor outputs and their amplitude increased as a function of speed. Although the wheel was run up to 2000 rpm, operation was unsatisfactory and therefore testing confined to under 1000 rpm.

4.2 MAGNETIC DESIGN ANALYSIS

4.2.1 Description

A simplified sketch of a test linear magnetic suspension block is given in Figure 4-3. The steady state bias flux is produced by two series high energy (Samarium cobalt) permanent magnets that are located in the stator magnetic circuit on sharp diagonals as shown. This maximizes magnet area and allows for minimum thickness. The flux crosses the air gaps to the rotor through a series of fringing sections. The rotor tends to seek minimum magnetic reluctance by aligning these sections thus providing passive restoring forces in the axial direction.

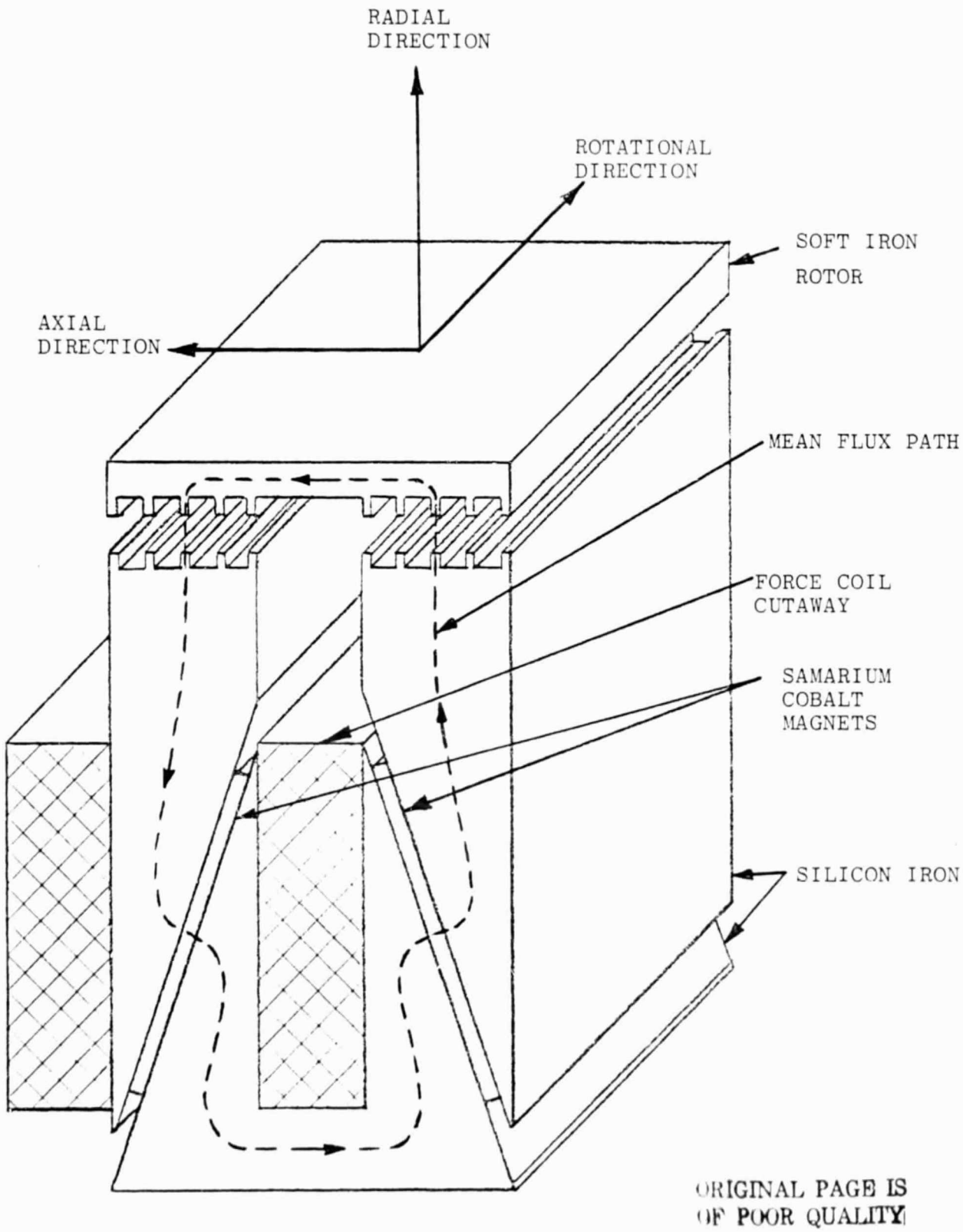

FIGURE 4-3

MAGNETIC SUSPENSION BLOCK

When there is alignment the axial force component reduces to zero.

A force of attraction always exists in the radial direction but this is actively controlled by the magnetomotive force (mmf) produced by the force coil (shown cutaway in Figure 4-3). Excitation to the coil modifies the steady state flux in the magnetic circuit and thus changes the radial force of attraction of the rotor. Since the coil produced flux must overcome the space occupied by the two magnets in addition to the two air gaps and the permeability of the magnets is near that of air, this necesitates that the magnets be as thin as possible.

The magnetic design is made with assurance that the force coil field cannot permanently demagnetize the high energy magnets. The magnets will always return the original level of flux to the magnetic circuit when excitation is removed and the original air gap is restored.

4.2.2 Design Analysis

The demagnetization curve for Samarium cobalt is approximately a straight line drawn through the coercive force H_C = 8000 oersteds and the residual induction B_R = 8000 gauss as shown in Figure 4-4. The operating point of the magnet is determined by the geometry of the magnetic circuit. This is represented by the shear slope line, B_D/H_D, and its crossing of demagnetization curve of the magnet give the operating flux density, B_D, and the field strength, H_D, of the permanent magnet.

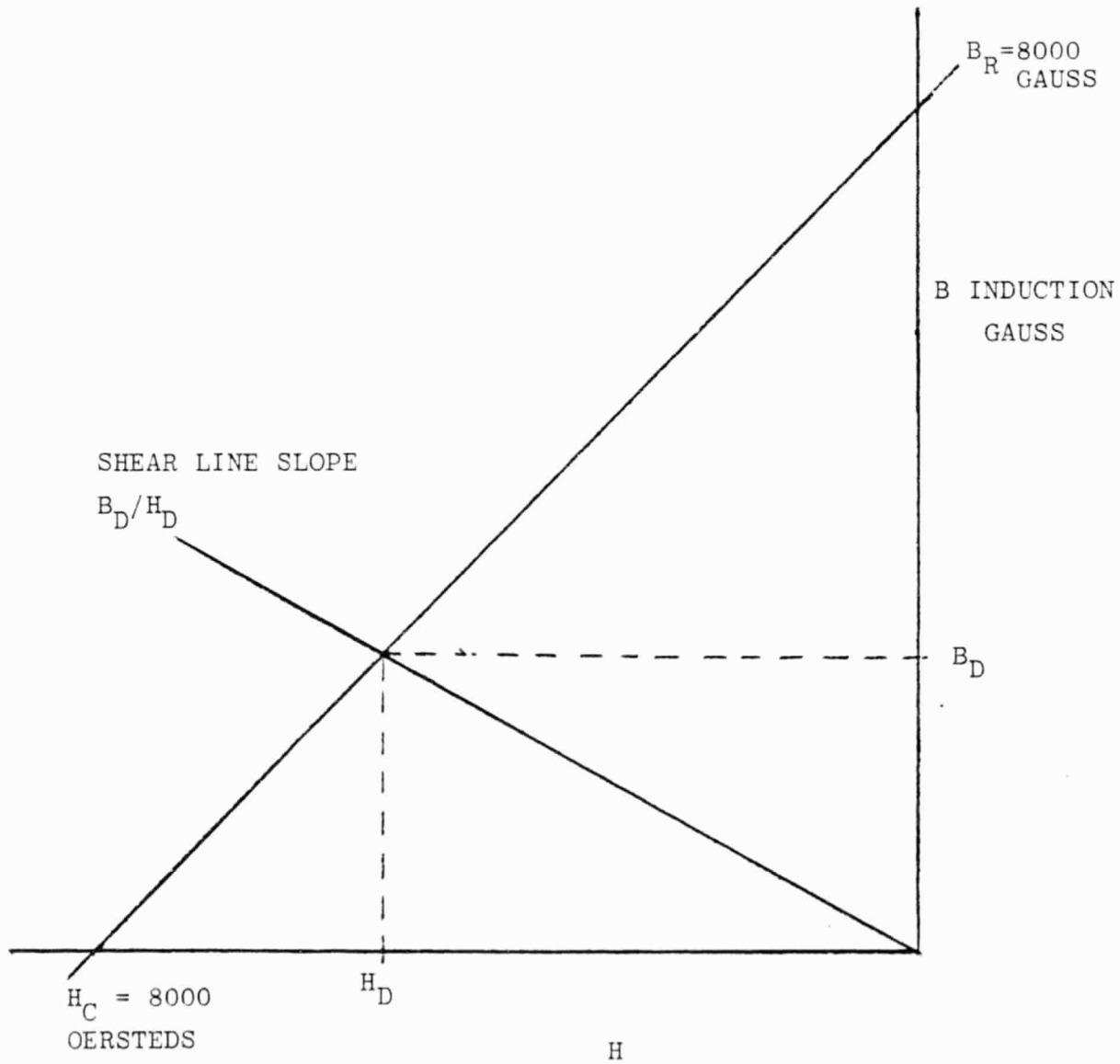

FIGURE 4-4

SAMARIUM COBALT MAGNET DEMAGNETIZING CHARACTERISTIC

4.2.2.1 $$B_D = \frac{B_R \frac{B_D}{H_D}}{\frac{B_R}{H_C} + \frac{B_D}{H_D}} \text{ gauss}$$

and the shear slope is given by:

4.2.2.2 $$\frac{B_D}{H_D} = \frac{F_L L_M A_G}{f_R L_G A_M} \frac{\text{gauss}}{\text{oersted}}$$

where

F_L = leakage factor

f_R = reluctance factor

L_M = length of magnets in direction of flux (cm)

L_G = length of air gaps in direction of flux (cm)

A_G = area of air gap (cm^2)

A_M = area of magnet (cm^2)

The flux produced by the magnets is:

4.2.2.3 $$\phi_M = B_D A_M \text{ lines}$$

The flux crossing the air gaps is:

4.2.2.4 $$\phi_G = \frac{\phi_M}{F_L} \text{ lines}$$

The flux density in the air gaps is:

4.2.2.5 $$B_G = \frac{\phi_G}{A_G} = \frac{\phi_M}{F_L A_G} = \frac{B_D A_M}{F_L A_G} \text{ gauss}$$

Combining equations 4.2.2.1, 4.2.2.2 and 4.2.2.5 yields:

4.2.2.6 $$B_G = \frac{B_R}{\frac{B_R}{H_C}\left(\frac{f_R L_G}{L_M} + \frac{F_L A_G}{A_M}\right)} \text{ gauss}$$

This equation is used to predict the air gap flux density knowing the magnet characteristics and the circuit geometry. The leakage and reluctance factors are estimated or approximated but since they are close to unity they may be omitted. Also with B_R = 8000 gauss and H_C = 8000 oersteds the equation simplifies to:

4.2.2.7 $$B_G = \frac{8000}{\frac{L_G}{L_M} + \frac{A_G}{A_M}} \text{ gauss}$$

This relation was used to scale an originally designed magnetic suspension block to the present design. Extensive tests were run on the original model with varying gaps, displacements, and fringing section configurations.

The force of a suspension block at the air gap in the direction of flux is given by the following equation:

4.2.2.8 $$F = \frac{6.45\ B_G^2 A_G (10)^{-6}}{72} (2) \text{ lb}$$

This relation with equation 4.2.2.7 is necessary for scaling to obtain the needed force at the air gap.

The axial force is not calculated with accuracy but is assumed to have a proportional relation to the radial force for a fixed fringing geometry. This is verified by test.

4.2.3 Test

For the present design a test magnetic suspension block (Figure 4-3) was fabricated for testing on a specially made fixture. The fringing geometry was predetermined by results on the original suspension block. The fixture was designed with linear bearings and guides which provided the means to measure linear forces in the axial and radial directions.

Measurements were taken of axial (passive) and radial (active) forces at various air gaps, displacements, excitations, and magnet thicknesses. The purpose of these tests was to determine the best air gap between rotor and stator and the thickness of the permanent magnet. These dimensions were determined with respect to (a) radial and axial support capacity, (b) radial and axial stiffness, and (c) critical speed defined by the radial stiffness and the anticipated mass of the rotor.

The results of the testing indicated that the air gap should be .025 inch and the permanent magnet thickness should be .060 inch. Some of the test derived curves are given in Figures 4-5 through 4-14.

Figures 4-5, 4-6 and 4-7 give the passive axial support force versus axial displacement at .020, .025, and .030 inch air gaps, respectively. The forces in each case tend to return the rotor to the zero axial position.

Figure 4-8 shows the passive axial stiffness in pounds per inch at .005 and .010 inch axial displacements versus

air gap length.

Figure 4-9 gives the radial force versus air gap length for .06 inch and .100 inch thick magnets at .025 inch axial displacement. These forces are in the unstable direction and increase as the air gap is reduced. The coil has to operate for control in this direction.

Figure 4-10 is the calculated axial sag by 24 pounds of force versus air gap for 8 suspension blocks. This is based on tests on a single suspension block.

Figure 4-11 is the radial force versus air gap on a suspension block with different levels of current in the coil.

Figure 4-12 gives passive axial force versus axial displacement for three air gaps.

Figure 4-13 shows the calculated critical speed versus air gap for the two magnetic lengths based on measurements.

Figure 4-14 shows the net radial force versus axial position for a gap of .020 inch and various coil currents.

Upon completion of analysis of the tests, the linear model was then redesigned to adapt to the rotational configuration of eight magnetic suspension blocks required for the 50 ft-lb-sec momentum wheel assembly.

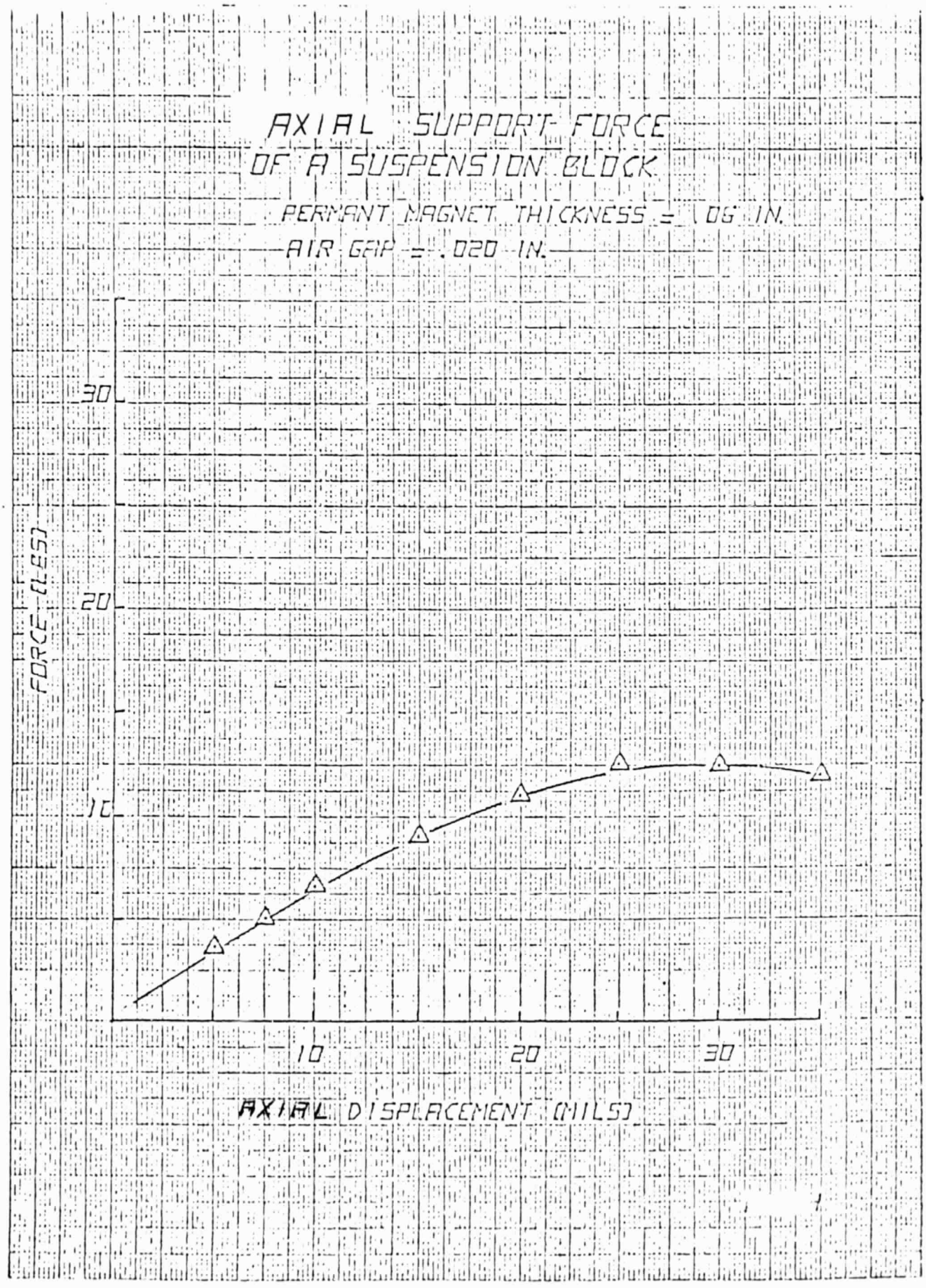

FIGURE 4-6

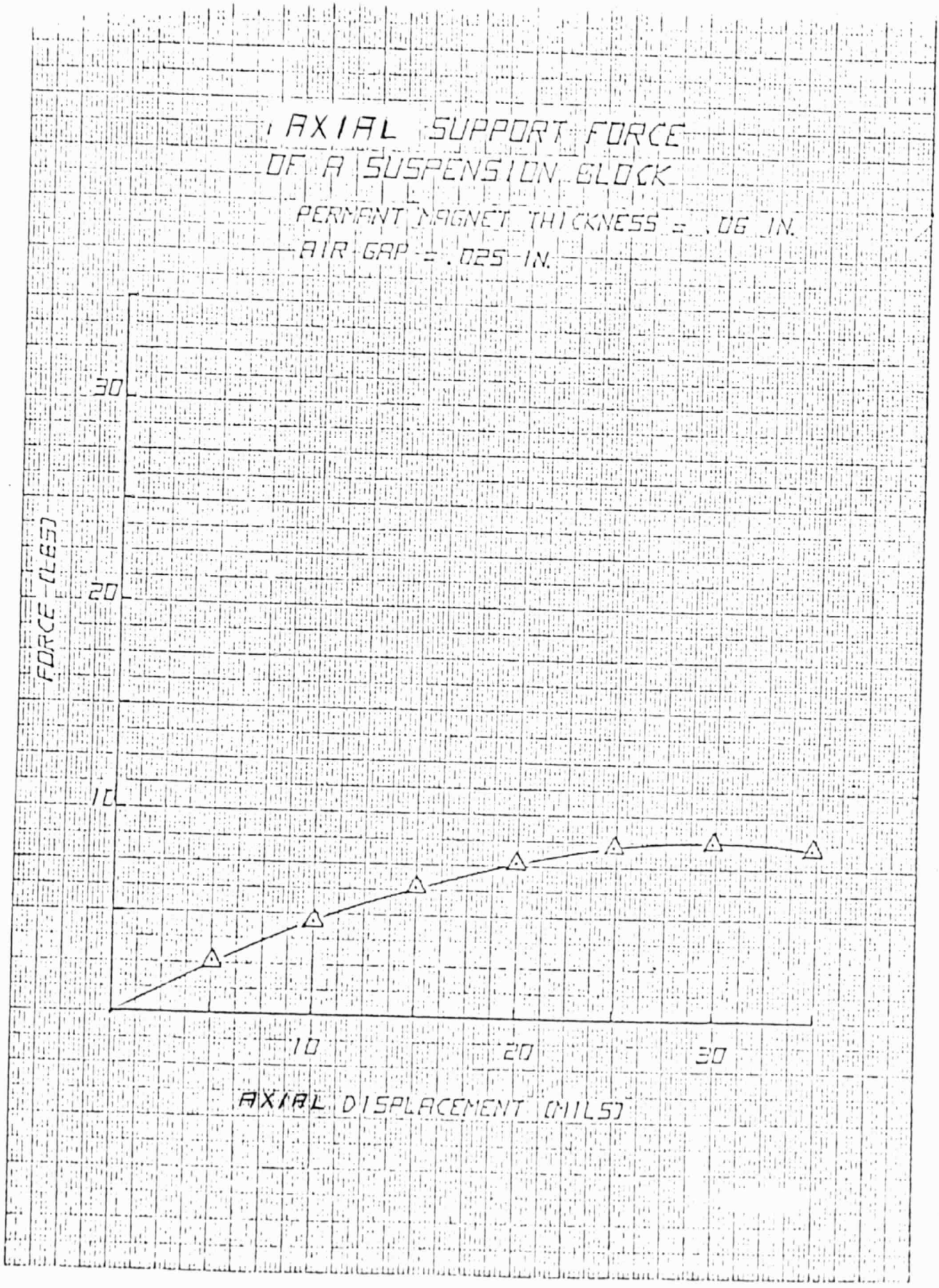
AXIAL SUPPORT FORCE
OF A SUSPENSION BLOCK
PERMANT MAGNET THICKNESS = .06 IN.
AIR GAP = .025 IN.
FORCE-(LBS)
30
20
10
10
20
30
AXIAL DISPLACEMENT (MILS)

FIGURE 4-6

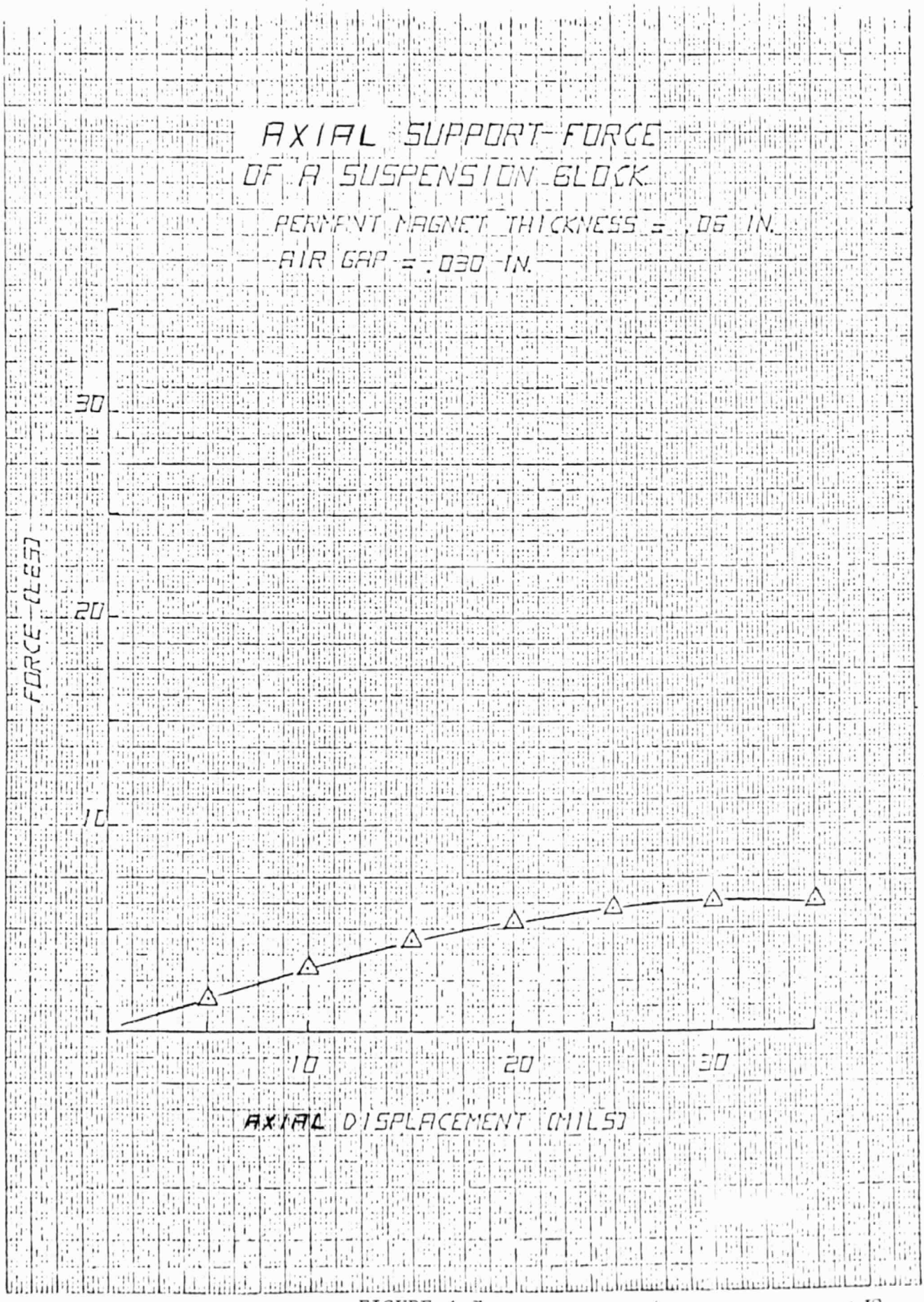

FIGURE 4-7

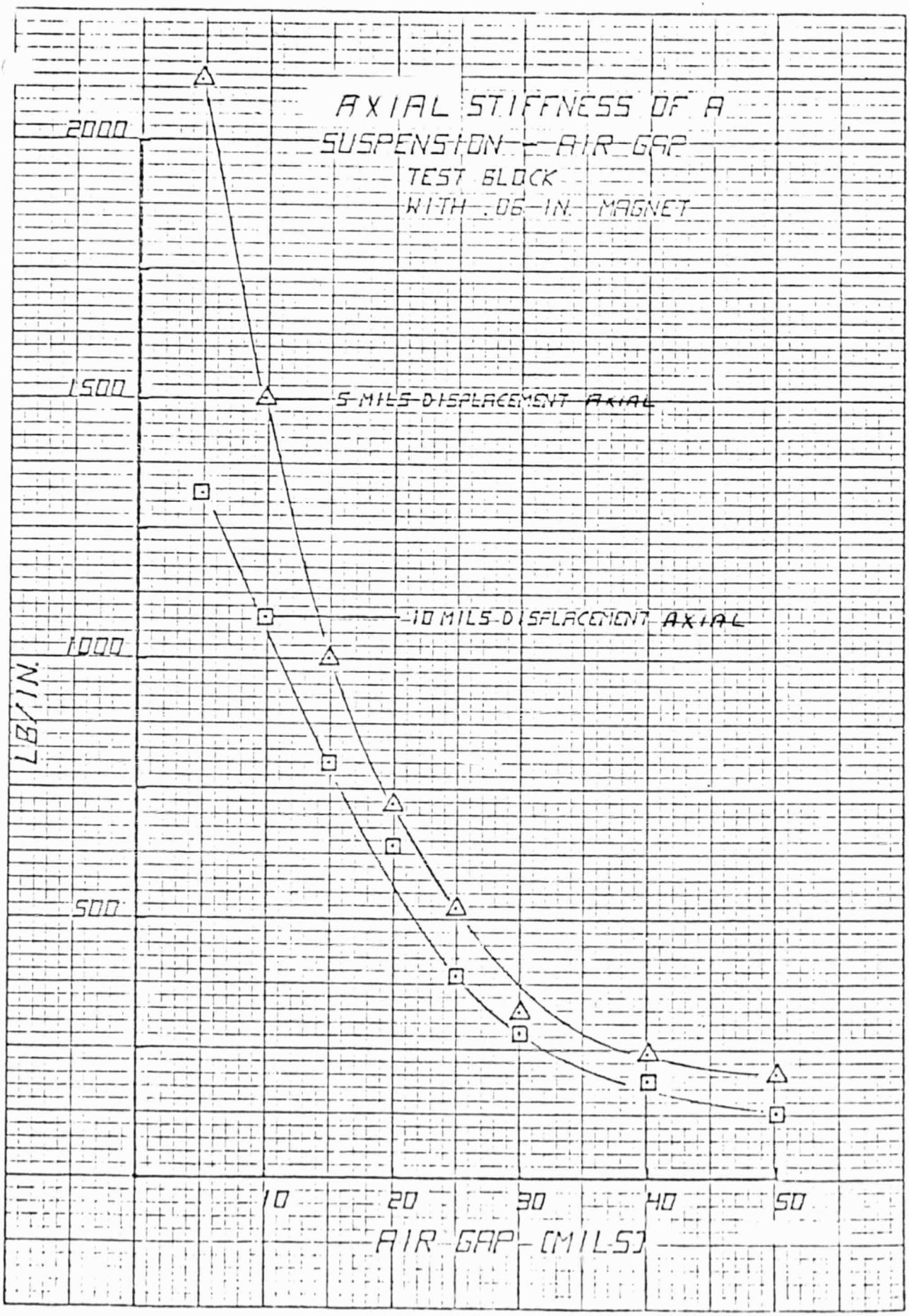
AXIAL STIFFNESS OF A SUSPENSION - AIR GAP
TEST BLOCK WITH .06 IN. MAGNET
2000
1500
1000
500
LB/IN.
5 MILS DISPLACEMENT AXIAL
10 MILS DISPLACEMENT AXIAL
10
20
30
40
50
AIR GAP - (MILS)

FIGURE 4-8

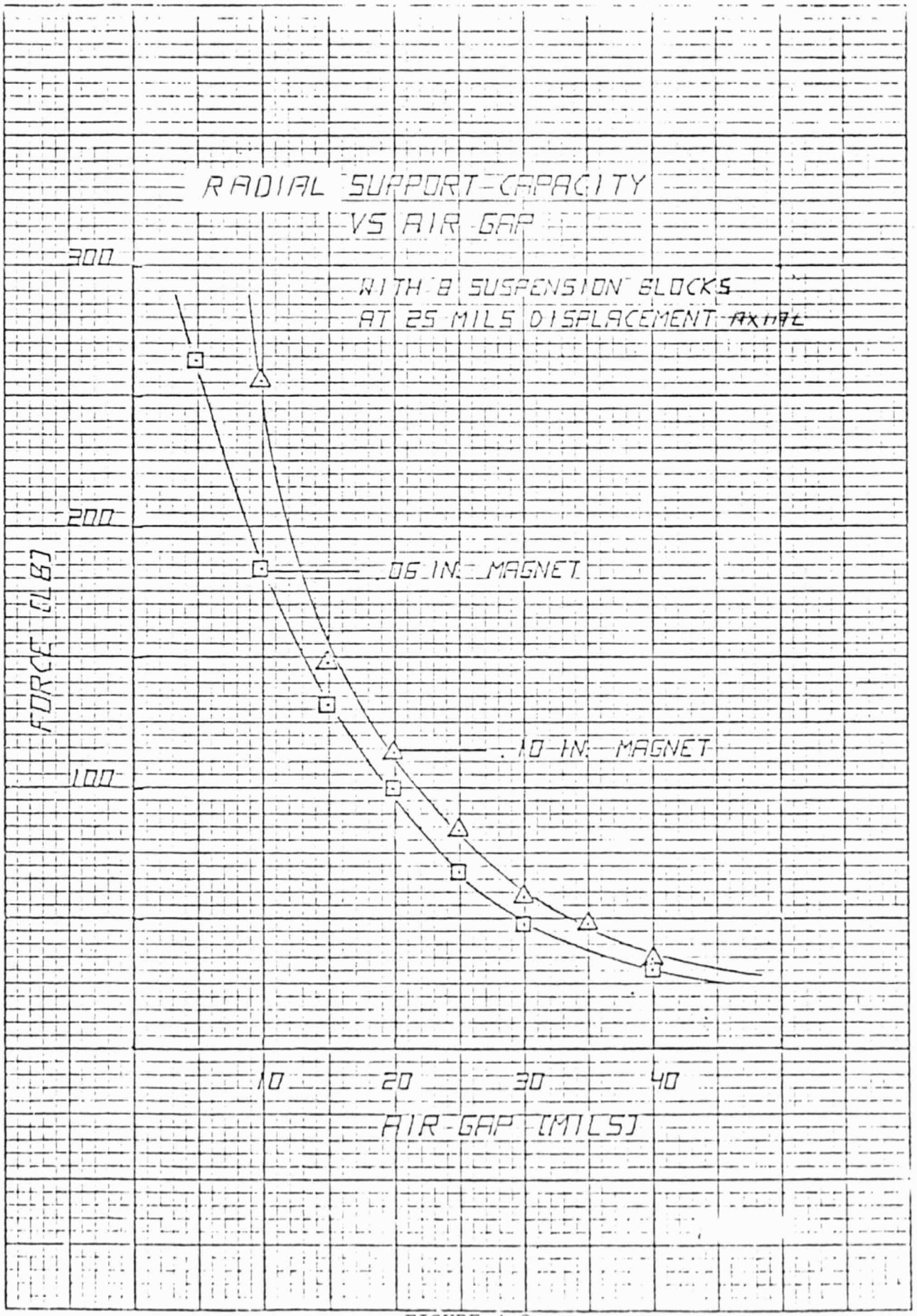

FIGURE 4-9

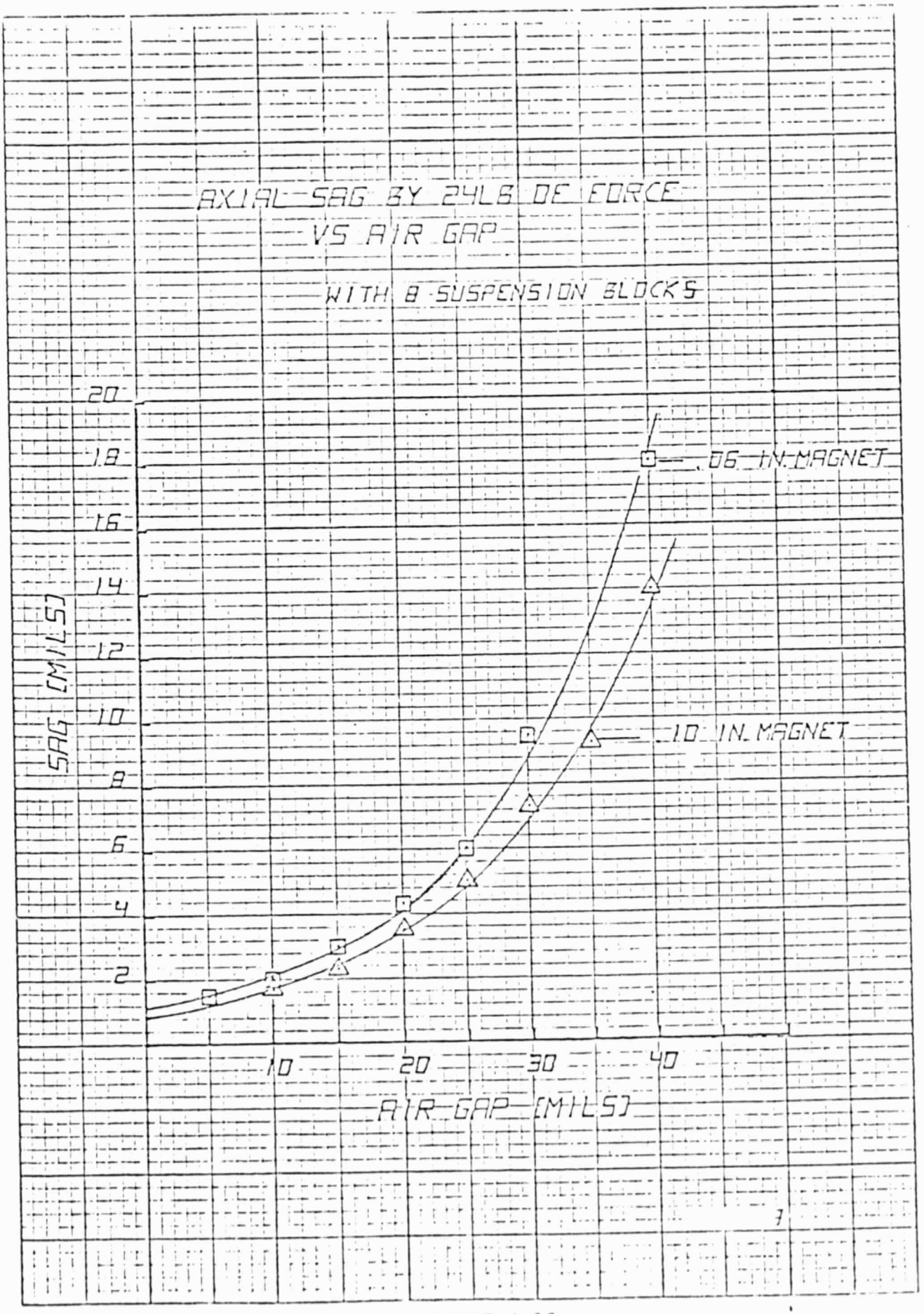
AXIAL SAG BY 24LB DE FORCE
VS AIR GAP
WITH 8 SUSPENSION BLOCKS
.06 IN. MAGNET
.10 IN. MAGNET
SAG [MILS]
AIR GAP [MILS]
20
18
16
14
12
10
8
6
4
2
10
20
30
40

FIGURE 4-10

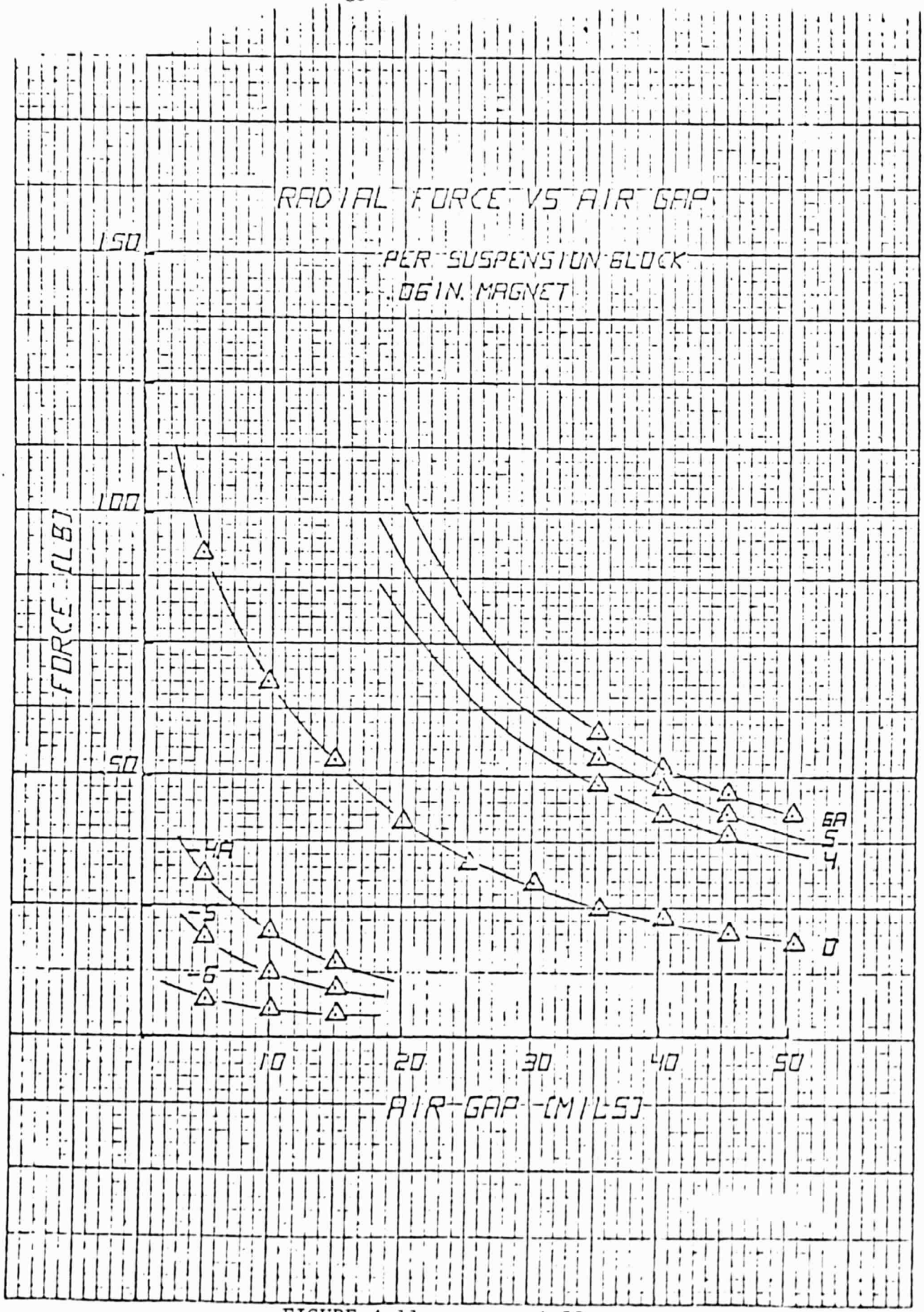

FIGURE 4-11

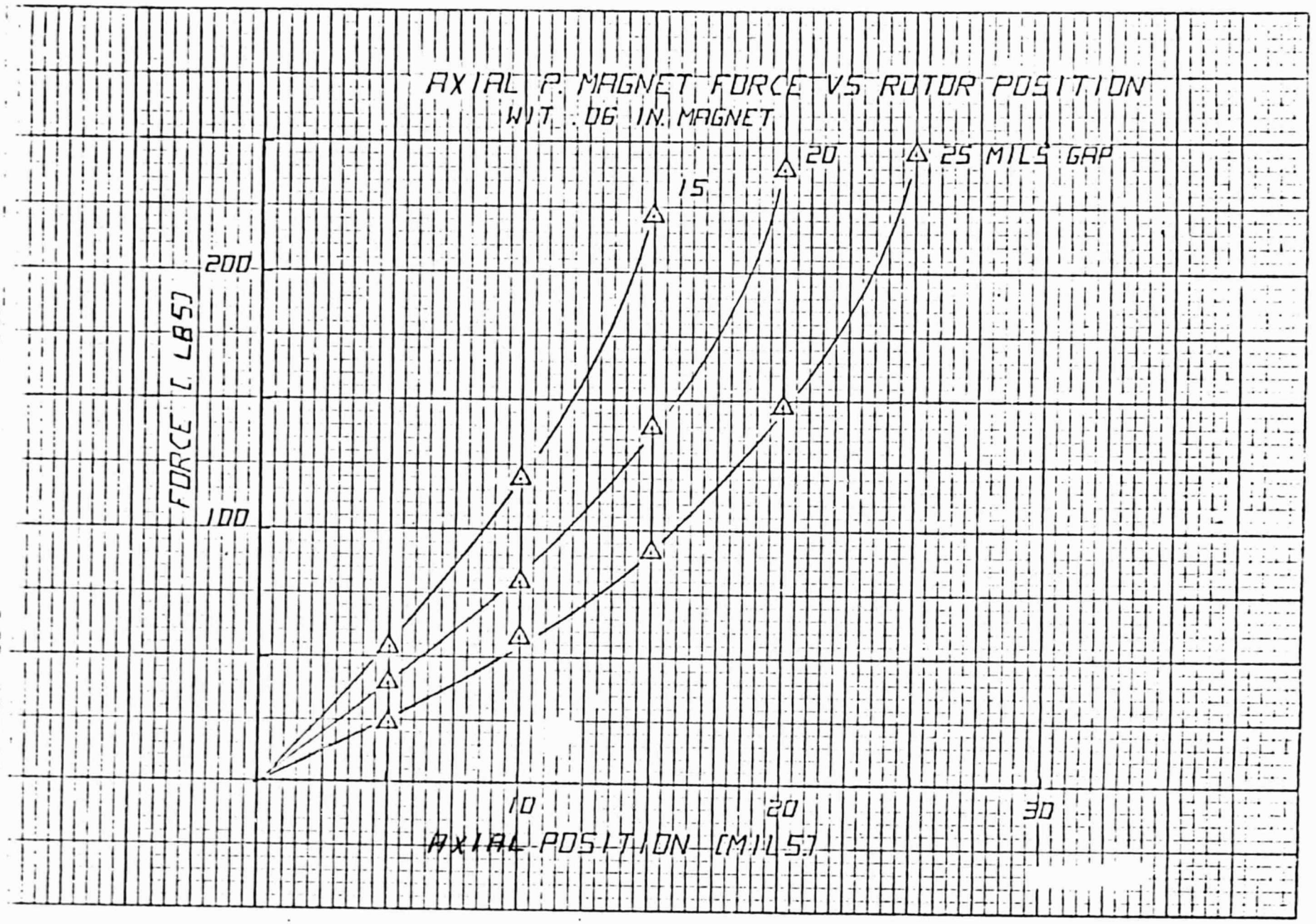
AXIAL P. MAGNET FORCE VS ROTOR POSITION
WIT .06 IN. MAGNET
25 MILS GAP
20
15
200
100
FORCE (LBS)
10
20
30
AXIAL POSITION (MILS)

FIGURE 4-12

CRITICAL SPEED VS AIR GAP
DUE TO RADIAL STIFFNESS
AT VZP OPERATION
5000
4000
3000
RPM
.10 IN. MAGNET
.06 IN. MAGNET
10
20
30
AIR GAP (MILS)

FIGURE 4-13

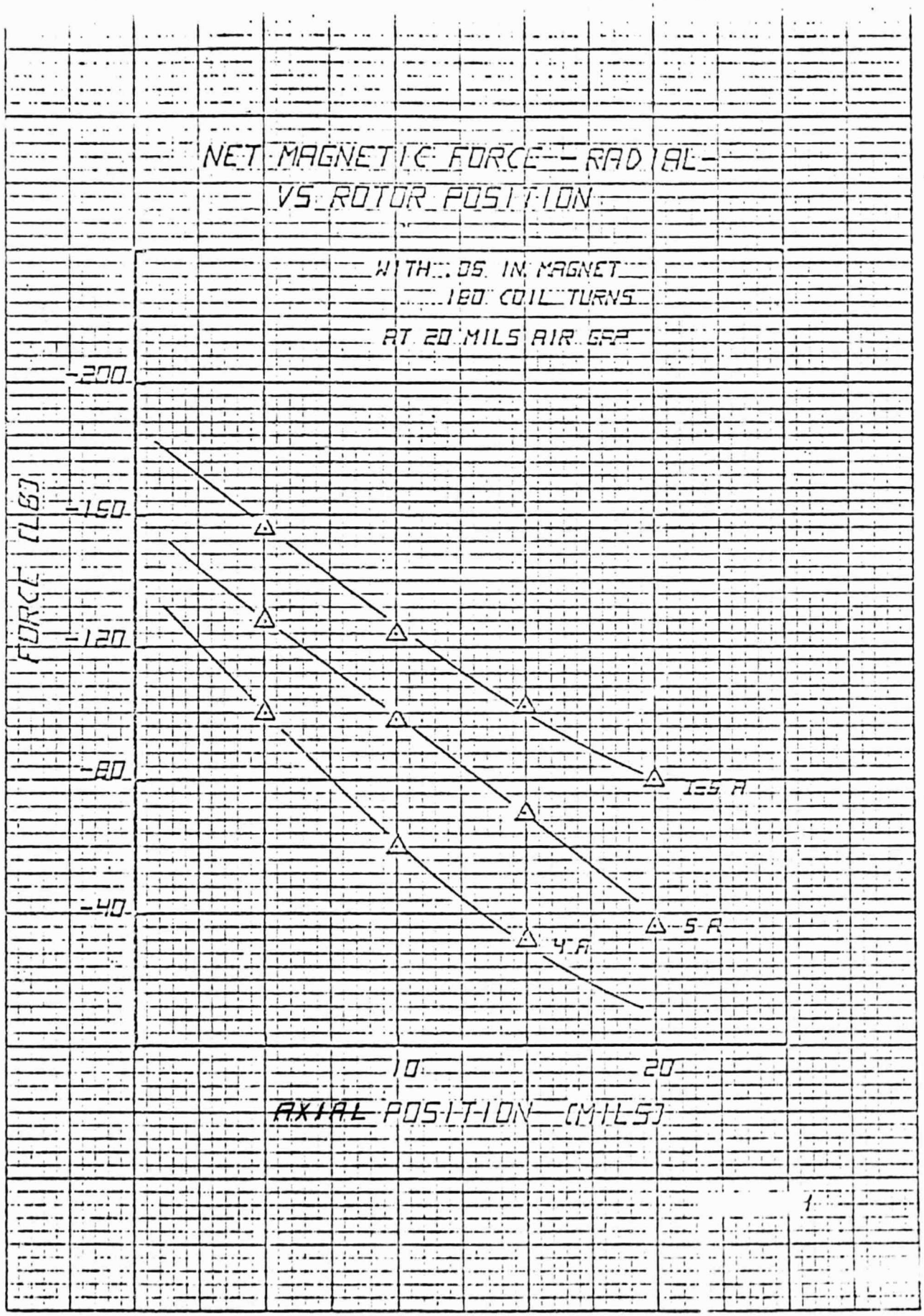

FIGURE 4-14

4.3 PERFORMANCE CHARACTERISTICS

The performance characteristics of the magnetic bearing suspension are summarized in Table 2-2 of Section 2.0. Except for magnetic drag torques, bearing parameters were generated by means of static testing. Bearing stiffnesses were the result of direct measurement. While measured forces were applied to the rotor, the rotors displacement was measured. This was done for both axial and radial stiffness measurements stiffness being simply

$$\text{Stiffness} = \frac{\Delta \text{ Force}}{\Delta \text{ Displacement}} \quad \text{(lbs/inch)}$$

The axial and radial support capabilities were calculated from the product of resultant bearing stiffness and allowable excursion.

The magnetic suspension drag torque was determined from prior data on the reaction wheel before the suspension was installed and data taken afterwards. Due to the units weight, drag torque data was taken by measuring coastdown speed rather than direct measurement on a torque cell. The digital torque data consisted of single wheel revolution times. The revolution time period was first converted to speed by

$$S = \frac{60}{P} \quad \text{(RPM)}$$

where P = period for one revolution

The drag torque was then computed from successive data points by

$$T = I\alpha = I \frac{2\pi}{60} \frac{\Delta RPM}{\Delta t} \text{ (oz-in)}$$

where I = wheel inertia = 36.5 oz-in-sec^2
ΔRPM = change in wheel speed
Δt = time between speed measurements

The resultant curve was then smoothed by least squares curve fit and is shown together with the motor drag curve from Section 5 in Figure 4-15. The motor drag when subtracted from this curve yields the magnetic suspension drag. The power required to overcome this drag is a function of speed and is computed from

$$P = \frac{S \times T}{1352} \text{ (watts)}$$

where S = wheel speed in RPM
T = torque in oz-in

Therefore the suspension drag of 1.9 oz-in at 1000 RPM is equivalent to a power demand of 1.4 watts. The ball bearing drag of 0.8 oz-in at 1000 RPM is equivalent to 0.6 watts.

The magnetic suspension was powered from a 26 volt DC source. The liftoff power required with the 0.007 ich radial touchdown gap was 150 watts. The power required with the wheel at rest was 1.4 watts. The powers were measured by measuring the current from the DC source.

MAGNETIC SUSPENSION DRAG TORQUE VS SPEED

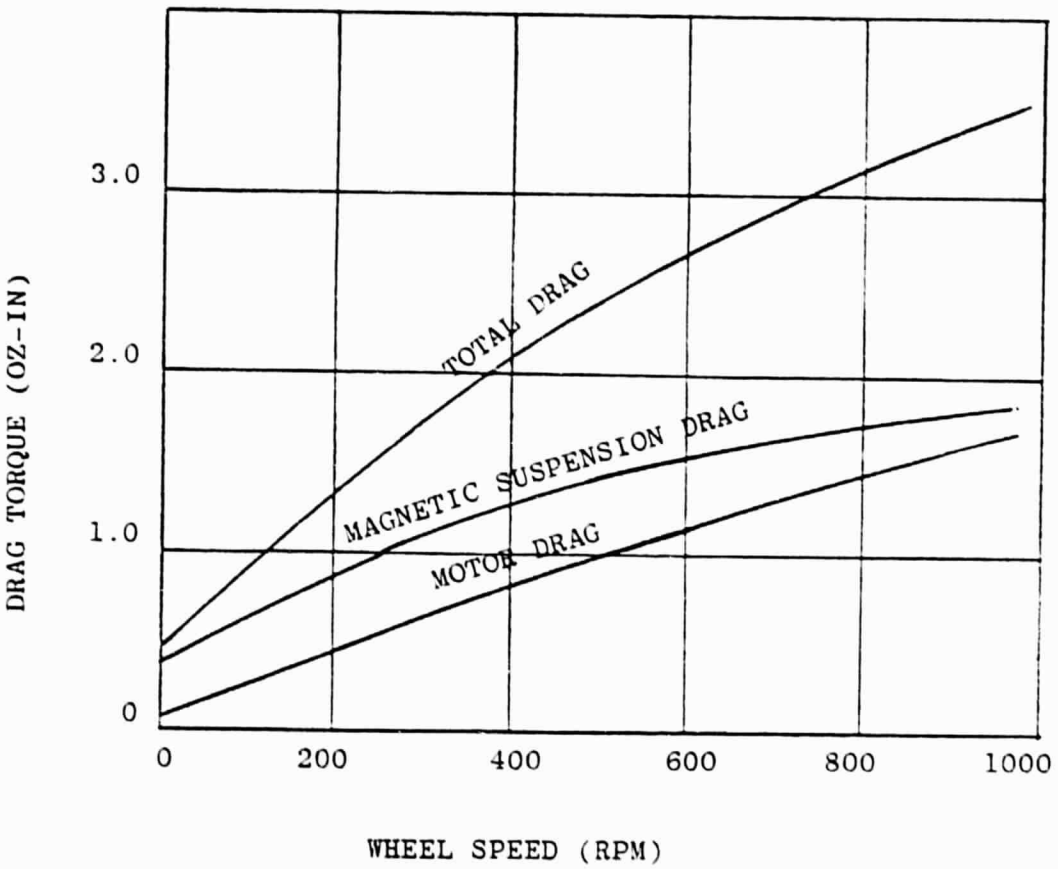

FIGURE 4-15

5.0 SPIN MOTOR DESIGN

5.1 SELECTION OF MOTOR TYPE

Conventional reaction wheels and momentum wheel are powered with AC induction motors. These motors are comprised of a two phase multipole wound stator and a squirrel cage rotor that is concentric with the stator and separated by a small air gap.

The ironless stator brushless DC motor is comprised of a stator that is wound on a nonmetallic form so that eddy currents cannot flow. The rotor consists of two concentric ring magnetic structures one of which contains the high energy permanent magnet pole pieces. The stator is located between the two rotor rings and is separated from each by air gaps. Commutation of this type of motor is done by hall effect devices embeded in the stator structure.

5.1.2 Reliability

The comparison of these two type of spin motors is summarized in Table 5-1. The feature that most favors the AC induction motor is its high reliability because of its simplicity of construction and operation.

The stator is simply wound on a magnetic core which acts as a good heat sink. The rotor circuit consists of a squirrel cage that is shorted at the ends and is located in a magnetic core that also acts as a good heat conductor.

TABLE 5-1

COMPARISON OF TYPES OF SPIN MOTORS

	AC INDUCTION MOTOR	IRONLESS STATOR BRUSHLESS DC
Favorable to AC		
Reliability	High	Medium
Commutation	Not Required	Hall devices
Equal AC & BDC		
Cogging Torque	None	None
Ripple Torque	Low	Low
Magnetic Drag Torque	None	Negligible
Favorable to BDC		
Efficiency	Low	Medium
Braking Power	High Power Input	Power Generation
Inverter	Required	Not Required
Torque Command	Proportional to voltage squared & dependent on speed	Proportional to current
Radial & Axial Forces	Appreciable	Negligible

The Brushless DC motor is more complicated in construction. The stator is not a good heat sink because its base is nonmetallic. The winding is simple as for the induction motor but the inclusion of commutation hall devices complicate the assembly at its terminations. The permanent magnets in the rotor are very favorably resistant to demagnetization, but they can pick up contamination or crack if not handled with care during assembly. The commutation electronics adds many components to the BDC system reducing the reliability.

However, if we include the conversion of the DC Buss to AC for the induction motor system, the reliability factor for the AC system will degrade bringing the two systems closer in reliability.

5.1.3 Operation

The basic reason for chosing a brushless DC system is its superior operating efficiency. The AC induction motor may have high efficiency if physical limitations are not imposed upon the design but this would be in a narrow speed range at best. The BDC motor, on the other hand, can have good efficiencies over a broad speed range. In addition, if electrical power can be extracted from the machine, this system can generate useful electrical power when braking. The AC induction motor system can only consume power under braking (plugging) conditions.

A very useful characteristic of DC & BDC machines is that torque is proportional to current. Generally, torque is being commanded and the stator current is the controlling parameter. For the AC induction motor torque is proportional to voltage squared if both phases are controlled simultaneously and the torque is also a function of speed. The design can be made to obtain certain torque speed characteristics but within basic limitations of induction motor characteristics.

5.1.4 Extraneous Torques & Forces

The ironless stator BDC motor has one design feature which makes it applicable for reaction and momentum wheels. It is the large air gap that is allowed when using the high energy magnets. This permits the stator to have no iron or other metal so that hysteresis and eddy current losses cannot be generated between the unexcited stator and the rotating rotor. Since there is no change in magnetic reluctance with rotation, there will be no cogging torque. Also, since there is no change of flux path in any metal with rotation, there will be no magnetic drag torque within the machine. The only drag may be produced if stray magnetic flux emanates from the machine and causes eddy currents to flow in nearby structure but this can be minimized by proper design.

The radial and axial forces of stator to rotor are also eliminated under no excitation conditions and are minimal when excited due to the large air gap and small magnetomotive force produced by the stator.

In comparison to the AC induction motor the ironless stator BDC motor is equal in cogging and magnetic drag. It is obvious that the unexcited AC machine should not develop magnetic losses because no magnetic fields are present. But when the machine is excited strong radial and axial forces may be produced which will be specially undesirable for magnetic suspension of the wheel.

The comparison should also be made between the conventional BDC motor and the ironless stator BDC motor. The conventional BDC motor has a stator wound in iron and a rotor with permanent magnetis. The air gap between them is generally small. This type of motor develops considerable cogging torque, magnetic drag, and radial and axial forces and is not suitable for reaction and momentum wheels.

The remaining undesirable torque is ripple which is produced with excitation. Since the stator produced magnetic field can only be introduced in discrete slots or locations of the windings, they will produce field harmonics which generate ripple torques. This is present in all machines and can be minimized by coil pitching, coil distribution, and skewing.

5.2 DESIGN ANALYSIS OF SPIN MOTOR

The design goal of the ironless stator brushless DC spin motor was to develop a torque of 70.7 oz-in up to a speed of 3000 RPM at 20 volts excitation and fit the motor in the Bendix 50 ft-lb-sec Reaction Wheel Assembly. In order to arrive at an optimized design, a computer program was devised that takes the number of poles, number of slots, coil pitch in slots, number of phases, maximum flux density in the iron, the wire current capacity in circular mils per amp and with basic dimensions arrives at a design. The basic dimensions are length, inside diameter, outside diameter, and magnet thickness and these are all allowed to take on appropriate increments.

The design process sets up the rotor magnetic circuit based on maximum densities and geometric conditions. The remaining magnetic air gap is then utilized to take as much stator winding of a predetermined wire size as possible.

The output of the program gives all the dimensions, areas, permanent magnet operating characteristics, air gap flux, winding information, torque constant, machine constant, current, and torque. By a visual comparison of torque and machine constant one can then select the best design for the trial inputs.

For this particular design dimensions were varied from a minimum inside diameter of 2.5 inches to a maximum outside diameter of 7.0 inches and a stator active length

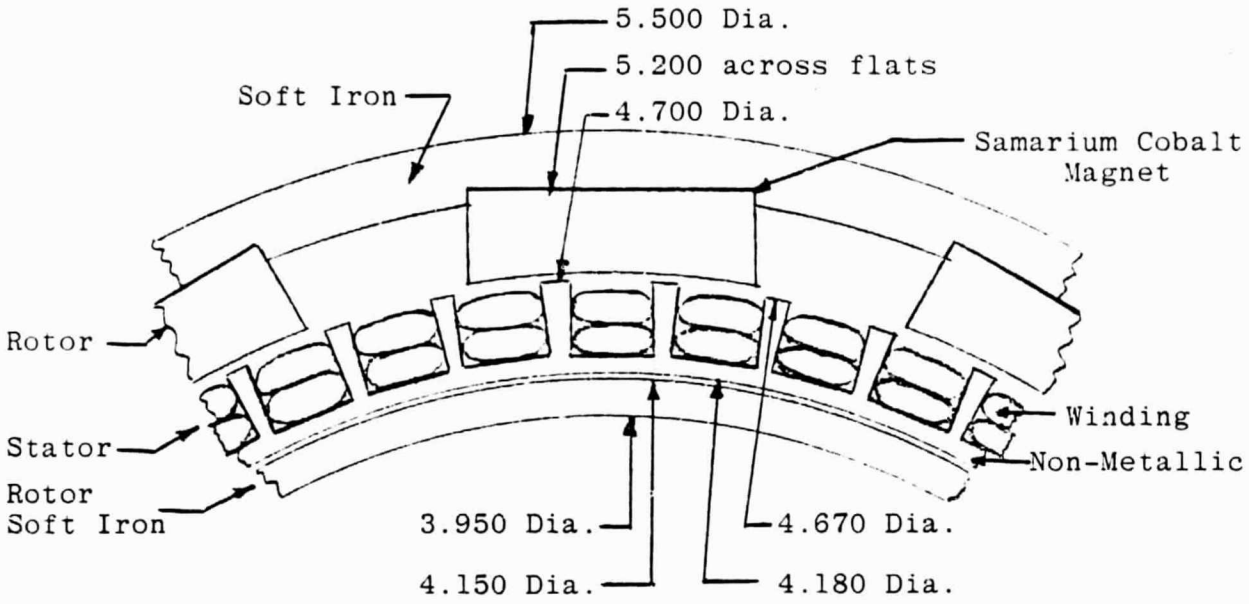

Number of Poles	=	12
Number of Slots	=	48
Coil Pitch	=	3 Slots
Number of Phases	=	2
Max Iron Flux Density	=	80,000 lines/in^2
Wire Current Density	=	250 Circular Mils/Amp
Outer Rotor Length	=	.700 in
Inner Rotor Length	=	.800 in
Stator Overall Length	=	1.8 in
Air Gap Flux Density	=	3320 Gauss
Turns of Wire per Phase	=	108
Wire Size	=	#28
Number of Parallel Strands	=	12
Resistance Per Phase	=	.197 ohms
Torque Constant	=	9.26 oz-in/amp
Back EMF Constant	=	.00685 volts/rpm
Machine Constant	=	20.9 oz-in/$\sqrt{\text{watt}}$
Current	=	7.56 amps
Torque	=	70 oz-in

IRONLESS STATOR BRUSHLESS DC DESIGN

FIGURE 5-1

to .85 inches max. A survey was made comparing machine of 6 poles through 24 poles and the best choice was used for this project. The design was selected on practical fabrication considerations in addition to the torque and machine constant. Figure 5-1 gives the pertinent information for the selected design.

5.3 DRIVE ELECTRONICS ANALYSIS

To obtain proper motor torque at all speeds, the motor current must follow the Hall voltage, in both amplitude and phase, at all frequencies up to maximum speed. A block diagram of the spin motor drive system is shown in Figure 5-2 where:

L = Motor inductance + Hall current sensor inductance + series load inductance = .33mH

R = Motor resistance + PWM power stage resistance + Hall current sensor resistance = .68 ohm

K_T = Motor torque constant = 8.35 oz-in/amp peak

K_b = Motor back emf constant = .00618 volts peak/rpm

Note that the Hall output voltage is assumed to be in phase with the motor back emf. Since it is required that the motor current (I_M) follow the Hall voltage (V_h) at all frequencies up to maximum speed, the drive electronics must be designed to minimize the motor current generated by the back emf (V_b). This problem is the conventional servo problem minimizing an unwanted disturbance, which means maximizing the values of G_2, G_4 and G_6 at all frequencies of interest. As the values

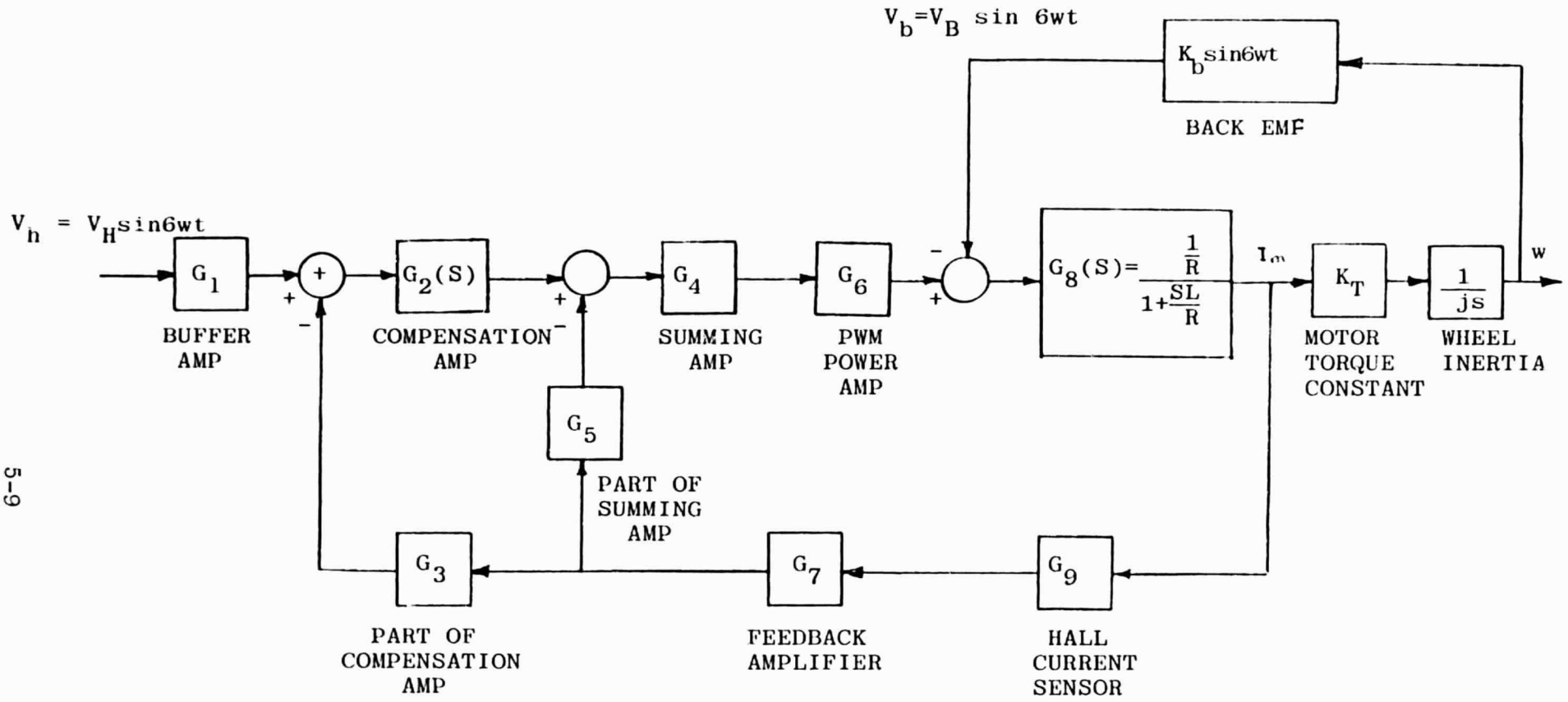

SPIN MOTOR DRIVE ELECTRONICS - BLOCK DIAGRAM

FIGURE 5-2

of G_2, G_4 and G_6 increase, however, the amplifier bandwidth increases. From a stability viewpoint, the maximum allowable bandwidth is set by the PWM power stage, which contributes a sampled-data-type phase lag. The PWM design used in the present system has a 19.2KHz effective sampling frequency, and the electronics are designed to produce a loop crossover frequency of 4000 Hz, or about 1/5 of the pulse-width-modulation sampling rate.

As a result, referring to Figure 5-1,

$G_1 = 10$ V/V

$$G_2(S) = 40 \frac{1+ \frac{S}{2\pi 2242}}{1+ \frac{S}{2\pi 20.2}} \text{ V/V}$$

$G_3 = 0.5$

$G_4 = 1.4$ V/V

$G_5 = .18$

$G_6 = 52$ V/V (for $B^+ = 28$VDC)

$G_7 = 10$ V/V

$$G_8(S) = \frac{1.47 \text{ A/V}}{1+ \frac{S}{2\pi 328}}$$

$G_9 = .03$ V/A

Using these values, the scaled block diagram of Figure 5-3 may be drawn. The open-loop transfer function, A(S), of the loop (for stability verification only) is

$$A(S) = (G_e+G_fG_h)G_cG_{de}\, e^{-\frac{ST}{2}}, \quad T = 1/19{,}200 \text{ sec}$$

where the transport lag approximates the dynamics of the pulse-width modulator.

Numerically,

$$A(S) = 647\, \frac{1+\frac{S}{2\pi 1137}}{(1+\frac{S}{2\pi 20.2})(1+\frac{S}{2\pi 328})}\, e^{-\frac{S}{38{,}400}}$$

A sketch of A(S) is shown in Figure 5-3. The crossover frequency is 4000 Hz and the phase margin is about 40 degrees.

The transfer function relating motor current to Hall voltage and motor back emf is

$$I_m = \frac{G_aG_bG_cG_dV_h - G_dV_b}{1+G_cG_dG_e+G_bG_cG_dG_f}$$

$$= \frac{66.0\, V_h(1+\frac{S}{2\pi 2242}) - 2.27\times 10^{-3}\, V_b\, (1+\frac{S}{2\pi 20.2})}{(1+\frac{S}{2\pi 2074})\,(1+\frac{S}{2\pi 2074})}$$

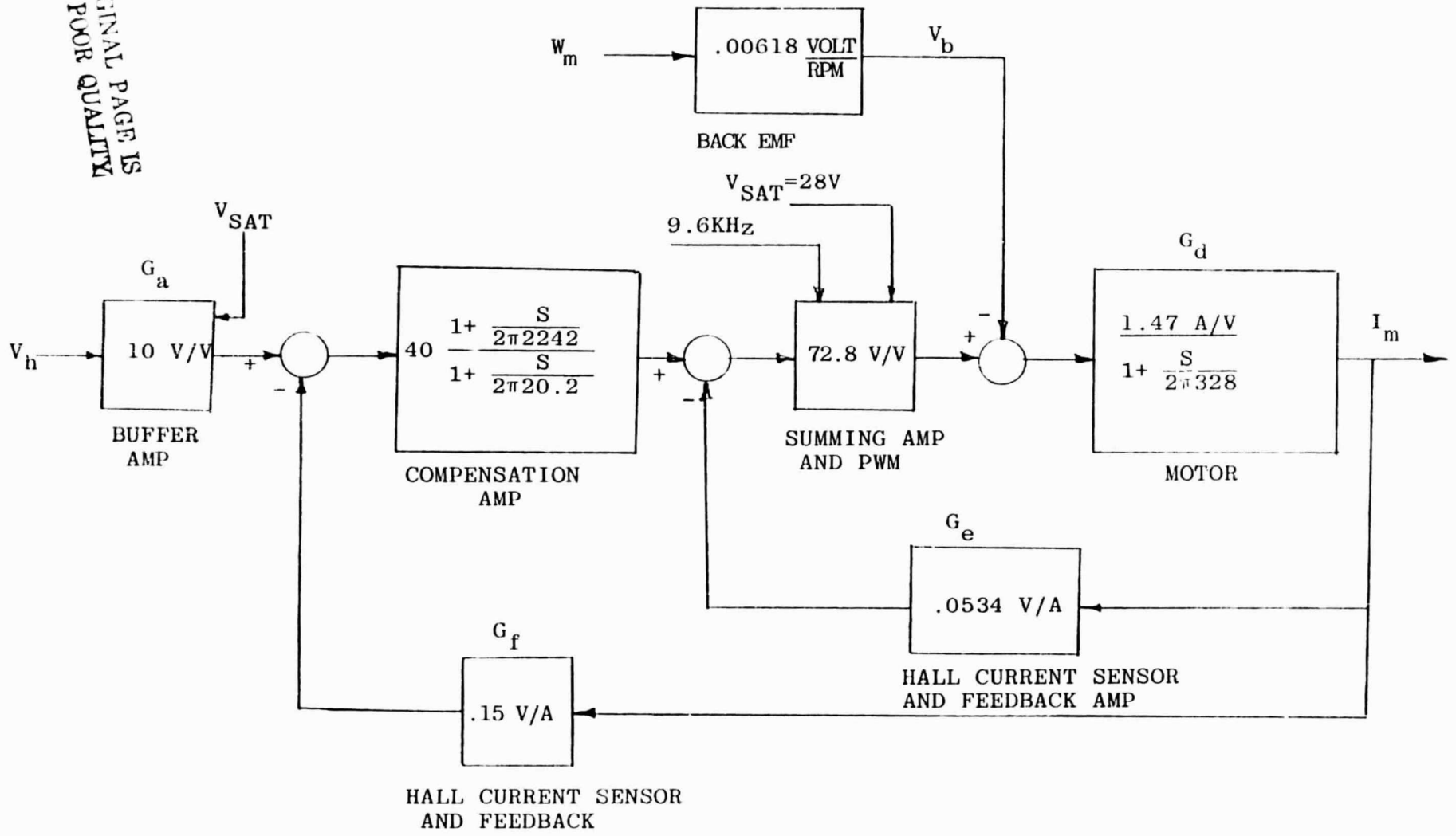

SPIN MOTOR DRIVE ELECTRONICS - SCALING DIAGRAM

FIGURE 5-3

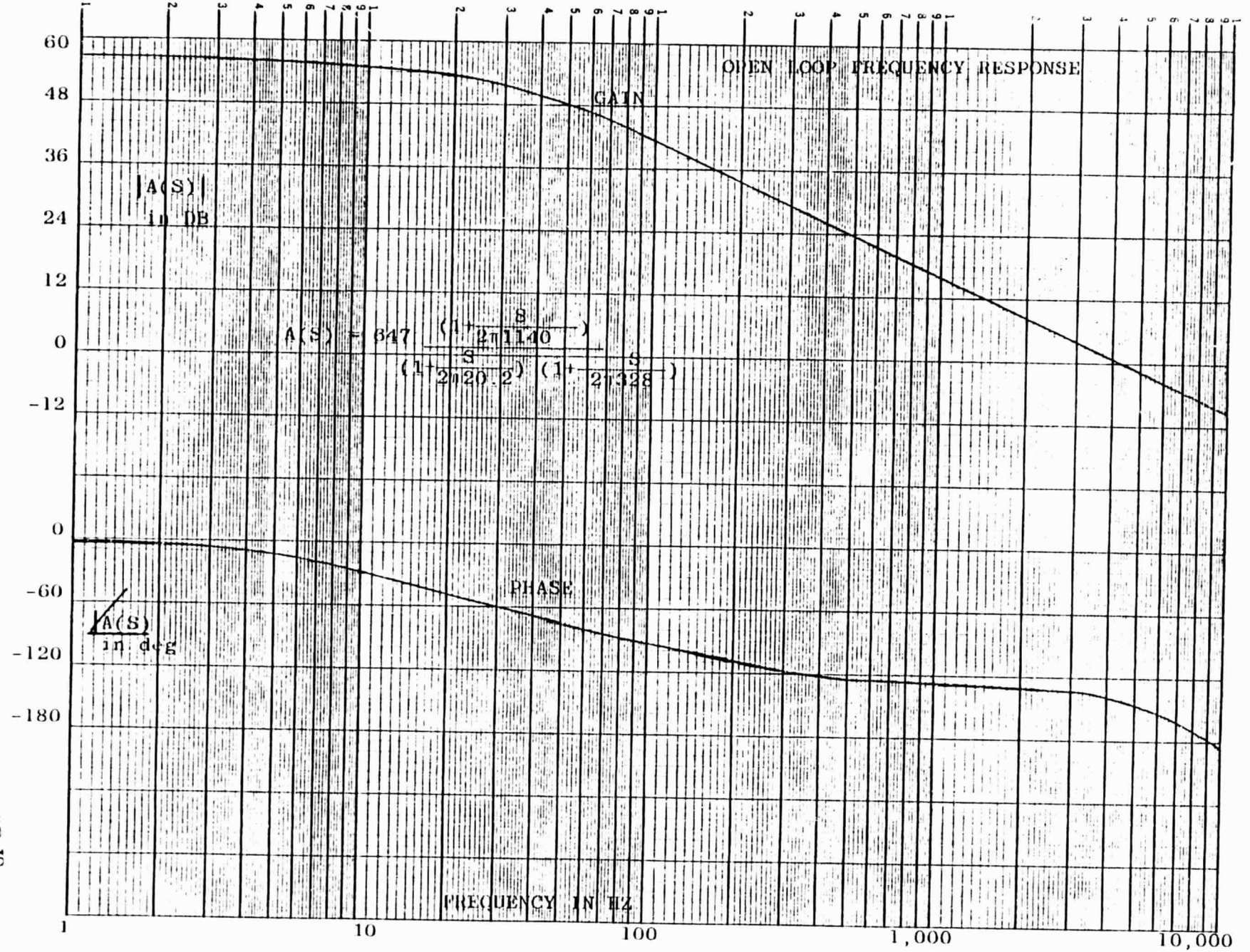

FIGURE 5-4

Since the developed motor torque is proportional to the magntiude of the component of I_m in phase with V_h and V_b (i.e. the real part of I_m), this last equation may be used for calculating torque roll off as a function of frequency. At 300 Hz (which corresponds to 3000 rpm) the motor back emf equals 18.54 volts. With a Hall voltage of .104V (corresponding to a torque output of 58 oz/in)

$R_e I_m = 6.688$ amps

At zero frequency, with $V_h = .104V$,

$R_e I_m = 6.864$ amps

Thus, the torque reduction due to frequency effects is 2.5% at 300 Hz, and the amplifier frequency response is adequate.

Up to this point it has been assumed that sufficient battery voltage is available to both overcome motor back emf and supply the current required to produce the commanded torque. The required battery voltage is given by the expression:

$$V_B = V_A + IR + K_b W$$

where:

V_B = required battery voltage

V_A = constant voltage drop in drive amplifier = 2V max

I = peak value of commanded drive current = 7.0 amp max

R = motor resistance + drive amplifier resistance + Hall current sensor resistance = .68 ohm

K_b = motor back emf coefficient = .00618 volts pk/rpm

W = motor speed = 3000 rpm max

Thus, for the condition of maximum current (i.e. maximum torque) and maximum speed, the required battery voltage = 25.3V.

5.4 SPIN MOTOR PERFORMANCE

The brushless DC motor was tested as part of a sub-system which included a Pulse Width Moduleated (PWM) Drive Electronics and a 50 foot-pound-second Reaction Wheel Assembly (RWA). The primary parameters of interest were reaction torque and power. The motors reaction torque was measured by suspending the RWA from a strain gage torque cell with the spin axis vertical. The natural resonance of the suspended spring mass system was 4.14 Hertz. This necessitating filtering of the torque indicators output with a 0.1 Hertz low pass filter. Since the RWA takes six minutes to change direction of maximum speed at maximum torque, this filtering was not considered detrimental.

Power measurements were made with a wattmeter which obtains a wattage reading by electronically multiplying the current signal by the voltage signal. Subsystem power measurements are easily measured since they are basically DC levels. The motor power measurements, however, posed a problem in that the voltage across the motor is pulse width modulated at a frequency of 4.8 kilohertz. Although the rated frequency response of the wattmeter is 2 kilohertz, it is believed that the wattmeter was responding with reasonable accuracy for these tests.

The RWA Drive Electronics was controlled by a speed controller using the RWA's 60 pulse two phase optical tachometer. The speed controller puts out a torque command voltage adjustable from 0 to ± 5 volts. The 5 volt torque command corresponds to maximum motor torque. The peak motor current was limited to 7 amperes thus limiting the maximum torque level to 58 ounce inches.

A repeatable bearing preload from unit build to unit build was accomplished using Belleville washers (springs) which were captured in special adjusting nuts, threaded into the Beryllium bearing support housings. These preload nut assemblies (two per unit), are adjusted so that the spring is approximately .005 inches from flat bottom. Once this deflection is achieved, a thrust load of approximately 9.0 pounds, based on the spring's spring rate, is applied to each bearing outer race in the spin axis horizontal position.

Since each preload washer still has .005 inch before the flat bottom position is reached, the flywheel has a total axial end shake of .010 inch. Therefore, a repeatable preload of approximately 9 pounds is achieved by always adjusting the preload nut assemblies to yield an axial end shake of .010 inches.

5.4.1 Torque Characteristics

The reaction torque characteristics of the subsystem are shown in Figure 5-5. The subsystem was operated at nominal buss voltage (28 VDC) and with five different torque command levels through four quadrants (modes of operation) arbitrarily designated,

I - Counterclockwise Acceleration
II - Clockwise Deceleration
III - Clockwise Acceleration
IV - Counterclockwise Deceleration

Quadrants I and II correspond to positive reaction torque output whereas quadrants III and IV correspond to negative reaction torque output.

The reaction torque values for the five torque commands in each quadrant were read from the curves every 200 RPM. A least squares straight line was then fitted to each set of data at each speed to determine the torque command scale factor. The coefficient of correlation was determined for each regression line with the lowest correlation being 0.997. The results of these computations are shown in Table 5-2. The total torque scale factor for all

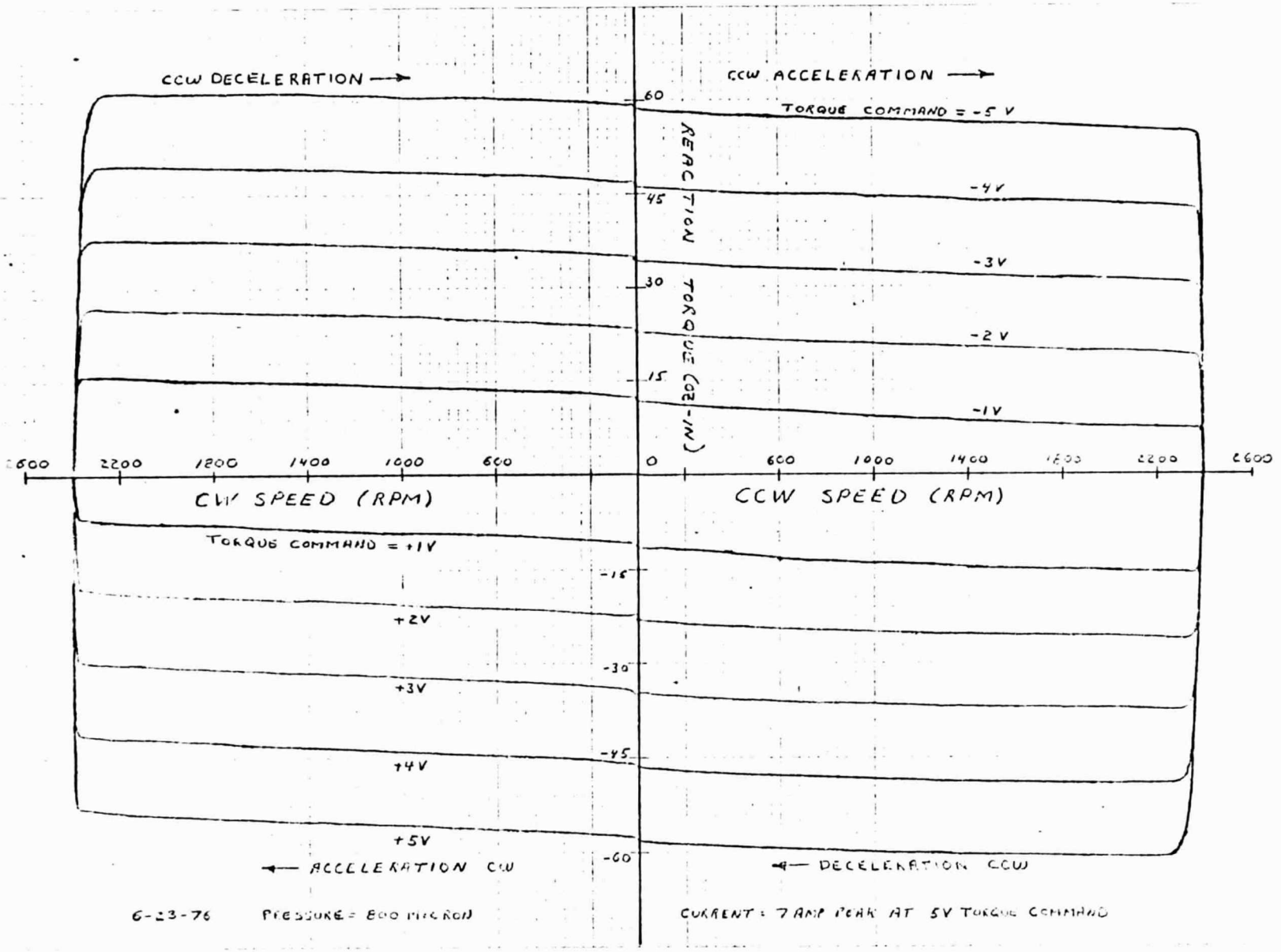

FIGURE 5-5

5-18

conditions is 11.66 ounce inch per volt $\pm$4.2% (3σ). The scale factors for positive and negative torques, respectively, are:

(+) 11.71 ounce inch/volt $\pm$4.2% (3σ)

(-) 11.60 ounce inch/volt $\pm$3.6% (3σ)

The above scale factors were determined from the reaction torque curves of Figure 5-1. The torque scale factors were also computed from the motor power curves (see Section 5.2) and are listed here to show concurrence of data.

(+) 11.36 ounce inch/volt
(-) 11.24 ounce inch/volt

It can be seen that there is less than 4% discrepancy between the two methods.

The drag torque losses of the RWA with the AC motor installed had been previously measured and approximated with a straight line as:

$$T_{AC} = 0.45 + 0.34 \times RPM \text{ (oz-in)}$$

where T_{AC} = drag torque with AC motor

RPM = motor speed in RPM x 10^3

Since the AC motor has essentially no magnetic drag losses and the wheel was run in vacuum, this drag can be associated with the ball bearings Coulomb friction and viscous drag.

The reaction wheel was disassembled, and fitted with the ironless stator brushless DC motor. The unit was re-assembled with the same bearings and tested under the same conditions as before. Drag torque curves were generated by measuring drag torques with a reaction torque indicator, computing torques from speed data and from the powered reaction torque curves. All of the curves were similar and combined into a composite drag torque curve.

The composite drag torque curve is considerably higher than the expected ball bearing torque. The composite curve is shown in Figure 5-6 along with the ball bearing curves. It is evident that there are more drag losses present than just ball bearing losses. As mentioned before, the composite curve was generated by several methods yielding similar results thus eliminating test error. Since the only functional change in the wheel had been in the motor, it of course became suspect. Since both the magnets and magnetic return iron are rotating, other sources of magnetic losses were examined. Metal parts near the rotating magnetis were remachined in nonmetallic materials with no effect. Another iron-less motor of similar design was tested on a smaller wheel but showed neglibible torques other than ball bearing drag torques. The inherent construction of the motor was examined and the cause for the additional drag discovered.

COMPOSITE DRAG TORQUE VS SPEED

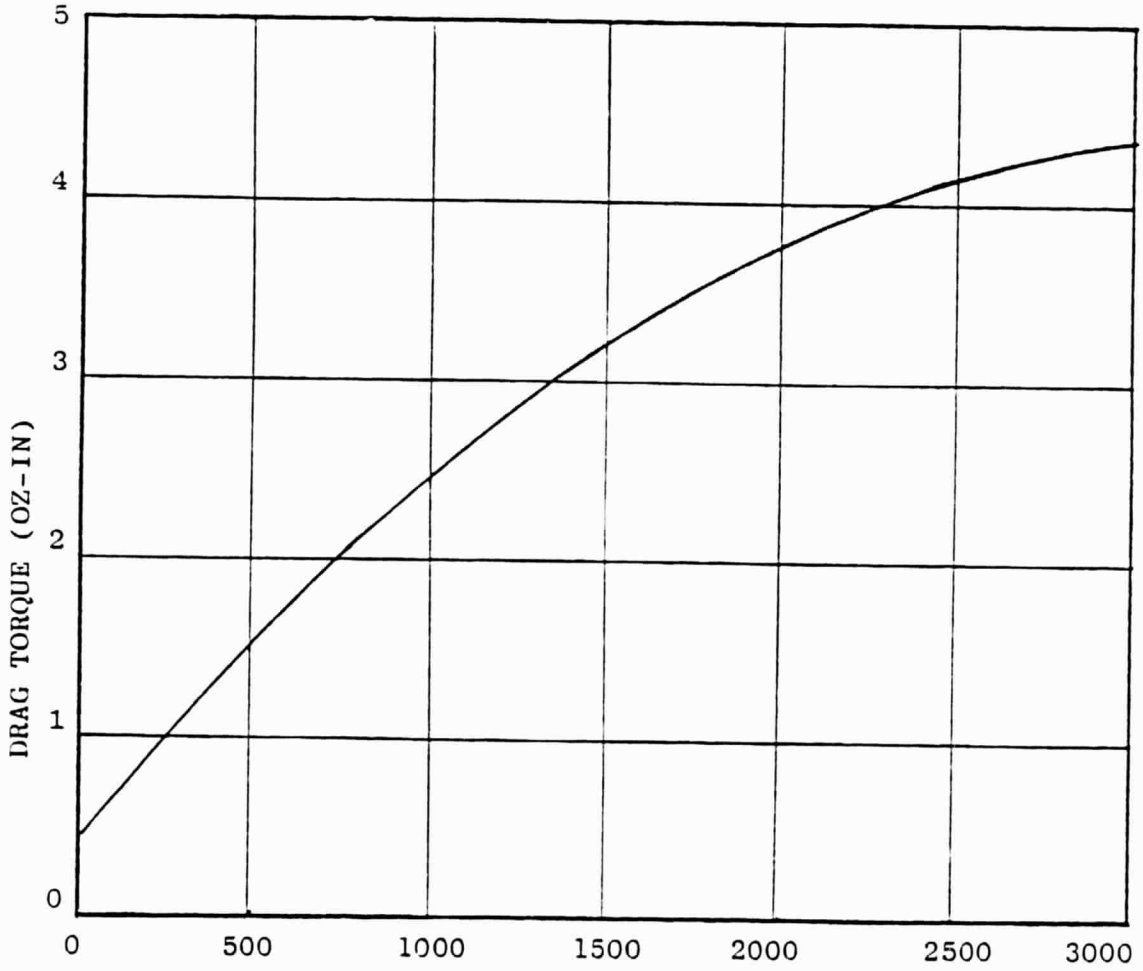

FIGURE 5-6

Due to the location and geometry of the motor windings and the parallel coil connections, it was possible for circulating currents to be generated within the motor. Although these circulating currents were originally thought to be of small value, they have proven to be otherwise. The circulating currents act as an electromagnetic brake on the motor thus causing the drag toques.

5.4.2 Power Characteristics

The sine and cosine motor phase powers were plotted against speed in the same manner as the reaction torque of Section 5.4.1. The data was also summarized in a similar fashion for computer analysis. (See end of Section for curves and tabulations). Least squares straight lines were fitted to the total motor power vs speed curve at each torque command level and for positive and negative reaction torques. The slopes of these lines were assumed to be directly proportional to the torque scale factor and another least squares straight line was fitted to the slope vs torque command data. The resultant slope represents the torque scale factor. Following are the scale factors for positive and negative torques, respectively:

(+) 11.36 ounce inch/volt
(-) 11.24 ounce inch/volt

Since the torque command voltage is proportional to motor current, the intercepts of power vs speed curves are proportional to the I^2R losses of the motor and wiring. Thus by setting the intercepts proportional to

the torque command voltage squared and fitting a straight line through these points, the I^2R constant can be computed. The peak current is approximately 1.4 amps per volt of torque command. Using the average I^2R constant of 2.0 watts/volt^2 and 1.4 amps/volt, the effective resistance of the motor is computed to be 0.50 ohms per phase. The measured DC resistance was 0.22 ohms plus an additional 0.49 ohms of AC losses totaling 0.71 ohms.

The steady state power of the subsystem was measured at zero speed and ±3000 RPM. The speed control circuit was used to keep the speed constant while the measurements were made.

Subsystem Power

Speed	28V
0	8.5
CW 3000	29.0
CCW 3000	26.9
0	7.4 (motor open)

Spin Motor Power

Speed	28V
0	0.6
CW 3000	11.8
CCW 3000	10.8

For the subsystem power at zero speed, the quiescent power is clearly proportional to the voltage squared thus representing I^2R losses in the electronics. The difference between zero speed and maximum speed subsystem powers should represent the spin motor power required at maximum speed. The measured spin motor powers, however, are higher by an amount partially accounted for by the I^2R losses of the 9.6 KHz PWM ripple current in the motor circuit. This is evident by comparing the subsystem power at zero speed with the motor in and out of the circuit.

The stable spin motor power is also representative of drag torque at constant speed. Using the spin motor powers at $\pm$3000 RPM and the motor torque constant developed earlier, the drag torque at 3000 RPM is computed to be 5.1 ounce inch which agrees with the measured drag torque.

5.4.3 Efficiencies

The reaction torque vs speed, drag torque, motor power and subsystem power curves mentioned in the previous sections were also used to compute various efficiencies. The motor efficiency was computed from the ratio of Required Power over Measured Power. The required motor power is computed from

$$P_R = \frac{T_M \, S}{1352}$$

where T_M = Motor Torque = Reaction Torque $\pm$Drag Torque

S = Speed IN RPM

The motor efficiency is

$$E_M = 100 \frac{P_R}{P_M} \%$$

The efficiencies were computed for each Torque Command Voltage from 1 to 5 volts every 200 RPM. The range of efficiencies was then plotted vs speed as shown in Figure 5-7. The motor efficiency is obviously zero at zero speed and is a function of speed. It is also a function of torque with the highest efficiency occurring at the lowest torque level. Thus, it can be seen that the motor is approaching 95% efficiency at maximum speed and low torque levels and 80% efficiency at maximum torque.

The subsystem efficiency was computed from

$$E_S = 100 \frac{P_R}{P_T} \%$$

where P_T = Total Subsystem Power

As above, the subsystem efficiency was plotted vs speed and is shown in Figure 5-6. The efficiency is again zero at zero speed and is about 55% at 2500 RPM. The tendency is for maximum efficiency at about 1/2 torque. The range of efficiencies with torque command is lower than the motor being generally less than $\pm 4\%$.

SPIN MOTOR EFFICIENCY VS SPEED

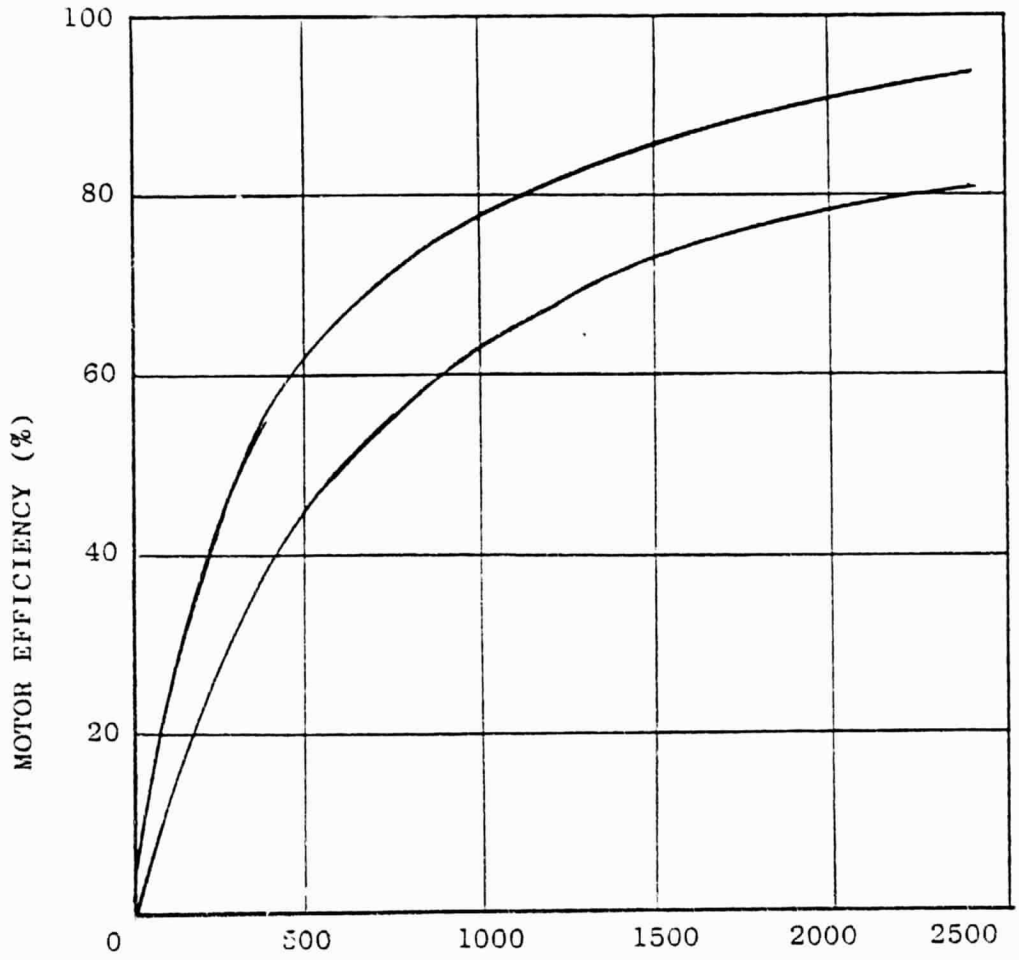

FIGURE 5-7

SUBSYSTEM EFFICIENCY VS SPEED

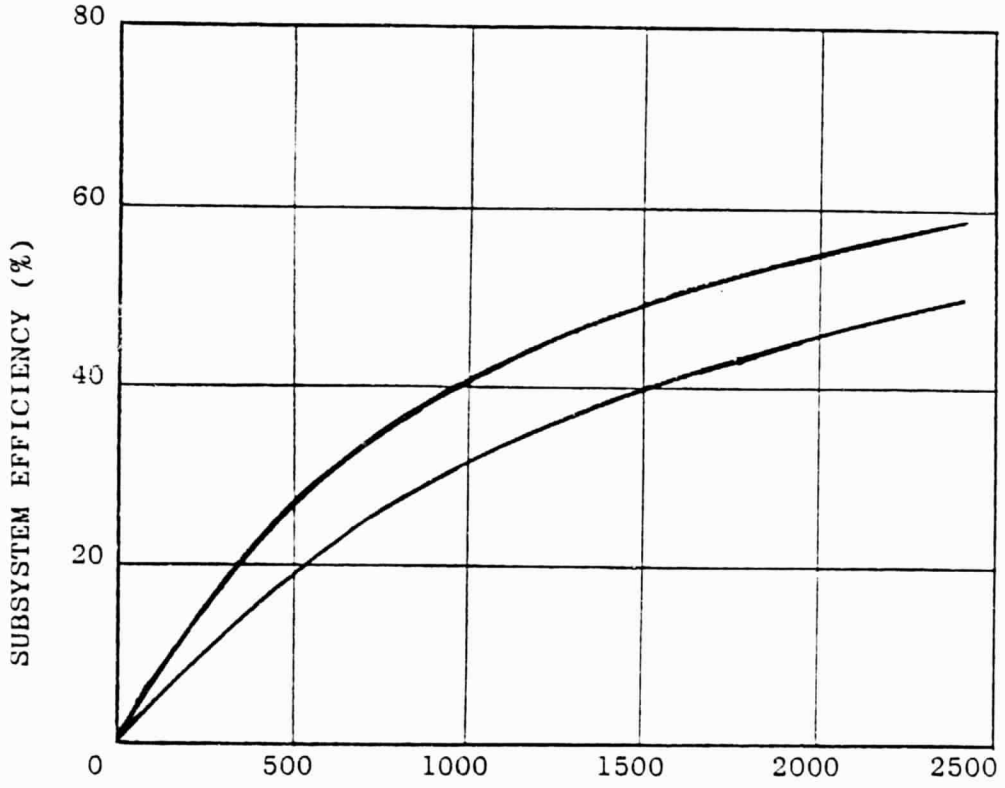

FIGURE 5-8

ELECTRONICS EFFICIENCY VS SPEED

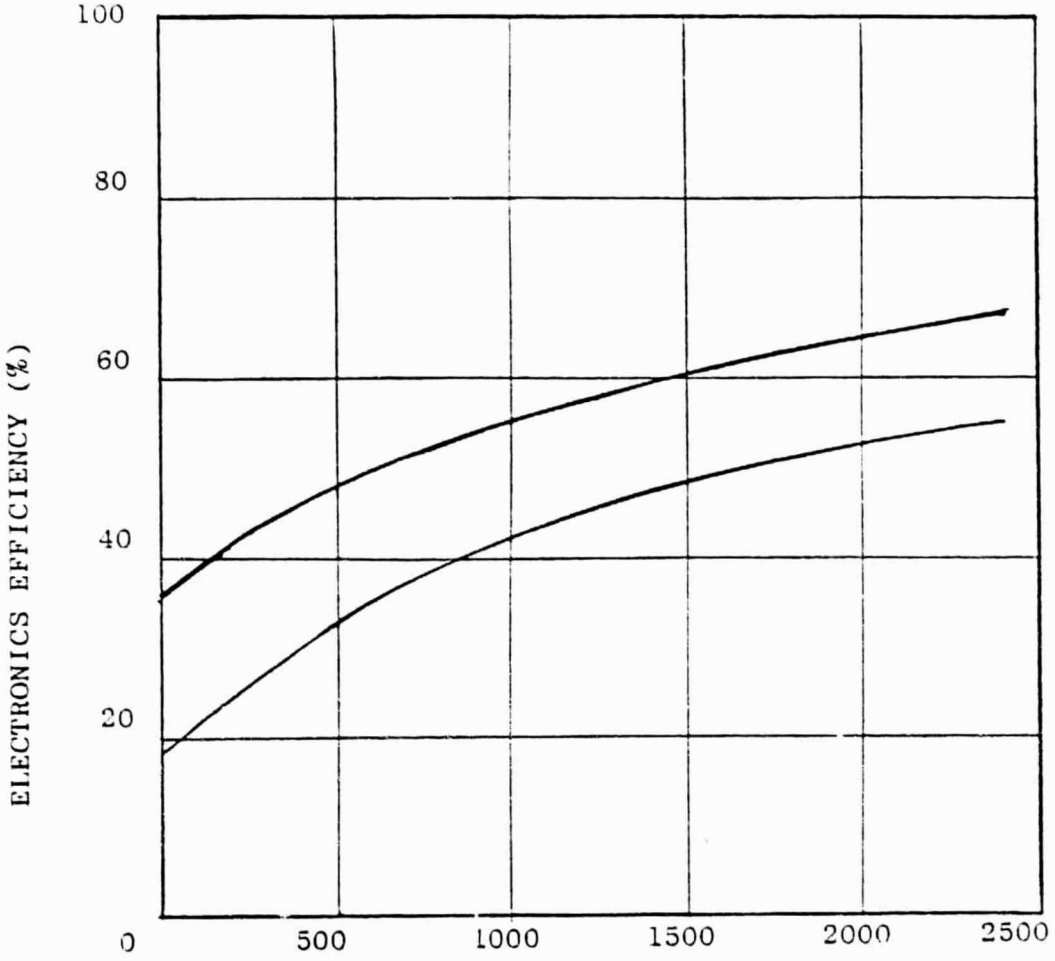

FIGURE 5-9

H-BRIDGE EFFICENCY VS SPEED

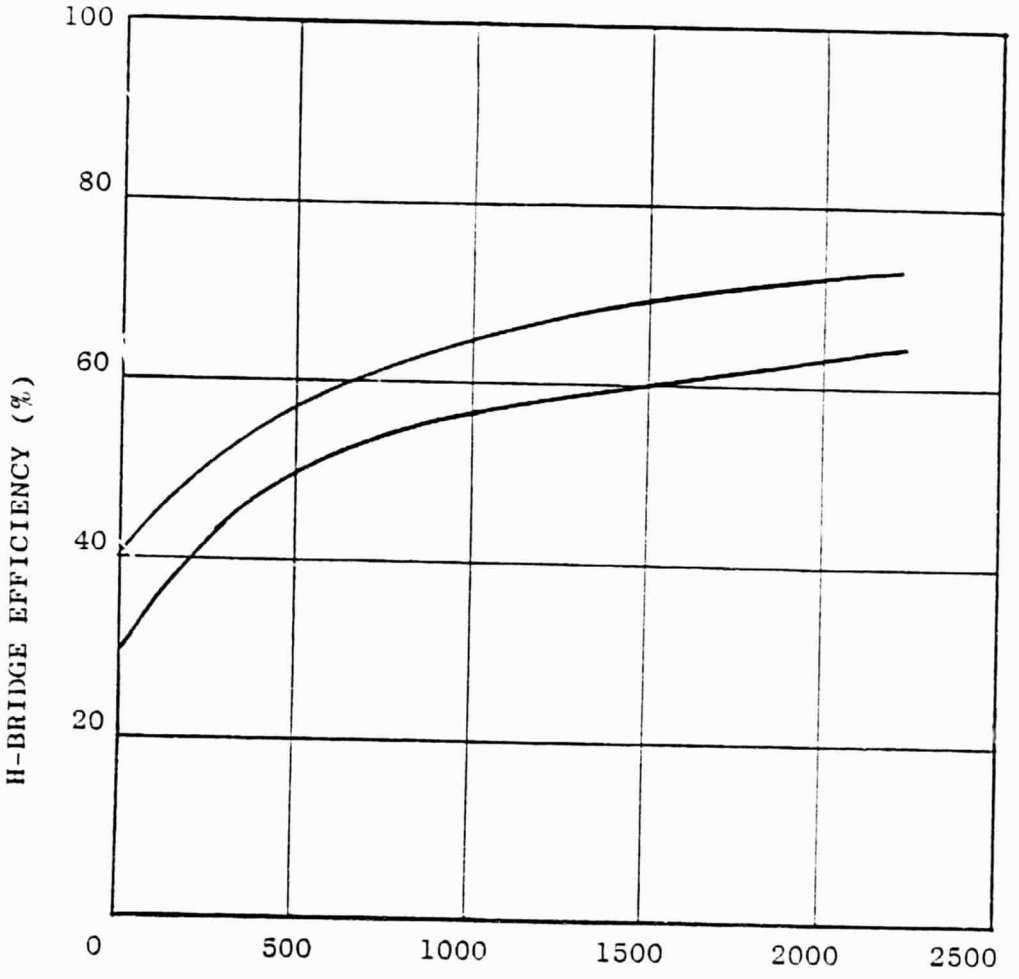

FIGURE 5-10

The electronics efficiency was computed from

$$E_E = 100 \frac{P_M}{P_T} \%$$

and is shown in Figure 5-7. The efficiency tends to dip down to about 30% at zero speed and rises to about 60% $\pm$5% at 2500 RPM. It should be noted, however, that the electronics are breadboard and were not designed to permit highest efficiency.

The quiescent power (P_Q) of the subsystem at zero speed was measured as 8.5 watts and this power was used to compute the effective efficiency of the H-Bridge or

$$E_H = 100 \frac{P_M}{(P_T - P_Q)} \%$$

The results are shown in Figure 5-8. The H-Bridge efficiency appears to be generally about 65% over most of the range and rising to 70% $\pm$5% at 2500 RPM.

The efficiencies of the electronics must not be taken two strongly since no attempt was made during circuit modifications at reducing power consumption. This was because the main objective of this study was the motor characteristics. Future circuits would naturally employ optimization techniques for increasing electronics power efficiency.

5.5 PERFORMANCE DATA

The performance data for the spin motor consists almost entirely of X-Y plotter curves. All the curves consist of either torque vs speed, torque vs time or power vs speed.

A computer was employed for the purpose of determining the spin motor characteristics from the torque and power curves. Four of the curves were used in this analysis:

Figure 5-11 Reaction Torque vs Speed
Figure 5-12 Subsystem Power vs Speed
Figure 5-13 Motor Cos Phase POwer vs Speed
Figure 5-14 Motor Sin Phase Power vs Speed

Vertical lines were drawn through the curves every 200 RPM and the values of intercepts with each curve coded for computer analysis.

The first data reduction consisted of fitting regression lines to the Reaction Torque vs Torque Command Voltage at each speed and each quadrant of operation (positive and negative torques and positive and negative wheel rotation). The motor torque was computed for each reaction torque with the equation:

$$T_M = T_R \pm T_D$$

where

T_D = Drag Torque = $0.46 + 0.00238S - .358 \times 10^{-6} S^2$

S = Speed in RPM

The required motor power was computed for each reaction torque from

$$P_R = \frac{T_M S}{1352} \text{ (watts)}$$

The resultant efficiencies for each point were computed from the following

$$E_M = 100 \frac{P_R}{(P_{SIN} + P_{COS})} \% = \text{Motor Eff.}$$

$$E_E = 100 \frac{(P_{SIN} + P_{COS})}{P_{TOTAL}} \% = \text{Elec. Eff.}$$

$$E_H = 100 \frac{(P_{SIN} + P_{COS})}{(P_{TOTAL} - P_Q)} \% = \text{H-Bridge Eff.}$$

$$E_S = 100 \frac{P_R}{P_{TOTAL}} \% = \text{Subsystem Eff.}$$

where

P_{SIN} = Sin Motor Phase Power

P_{COS} = Cos Motor Phase Power

P_{TOTAL} = Subsystem Power

P_Q = Quiescent Power = 8.5 watts

The efficiency data was then summarized in Table 5-2. The data computed from the regression lines of Reaction Torque vs Torque Command Voltage at constant speed

was summarized in Table 5-3. In addition, a regression line was fitted to the intercepts of these regression lines. Also, an average and standard deviation were taken of the slopes.

The total motor power was summarized in Table 5-4. Regression lines were fitted to the Power vs Speed data points for each Torque Command Voltage and both positive andnegative torques. The slopes of the regression lines vs torque command voltage were themselves fitted to a regression line. The intercepts of the straight lines vs torque command voltage squared were also fitted to a regression line.

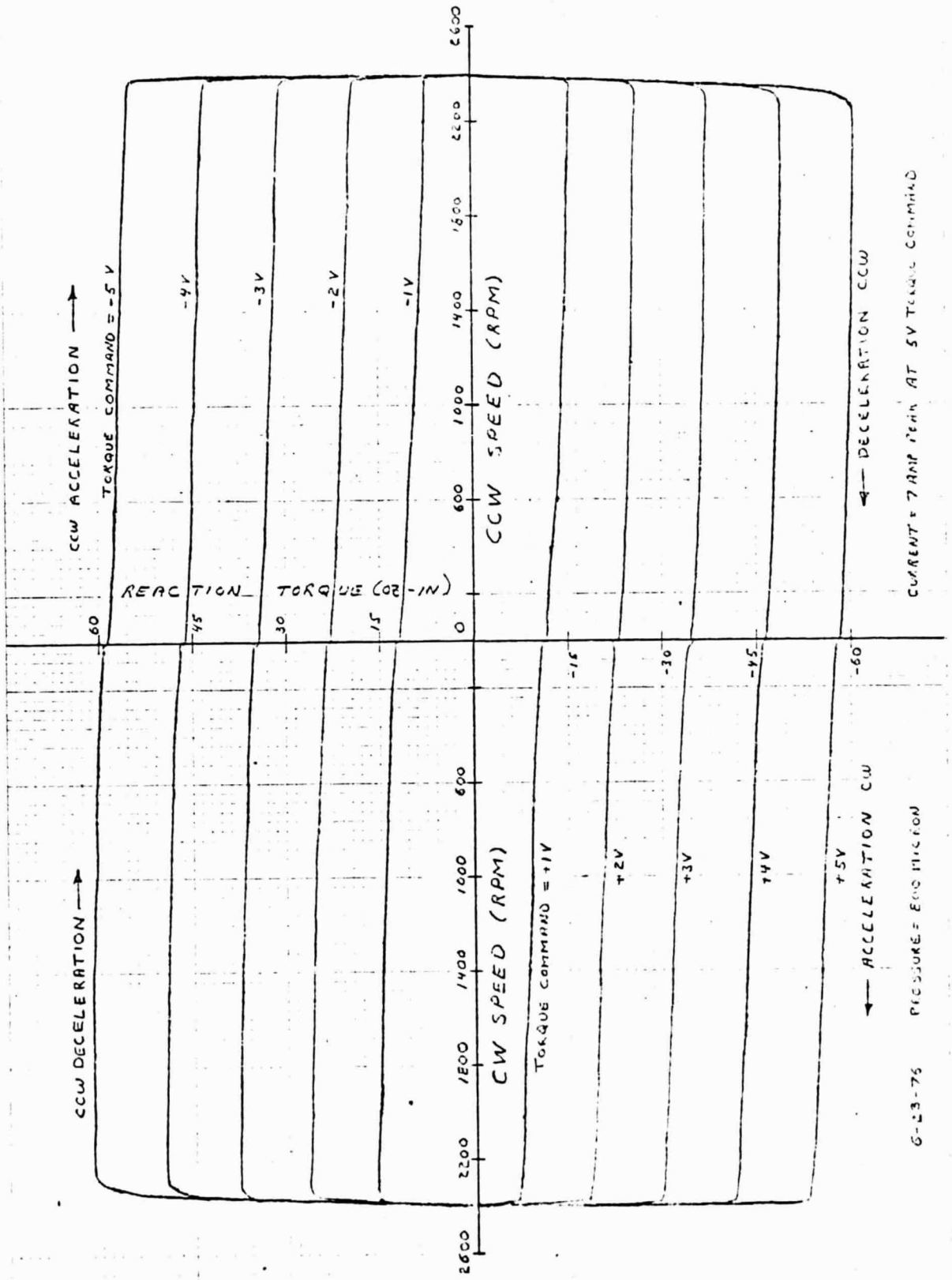

FIGURE 5-11

ORIGINAL PAGE IS
OF POOR QUALITY

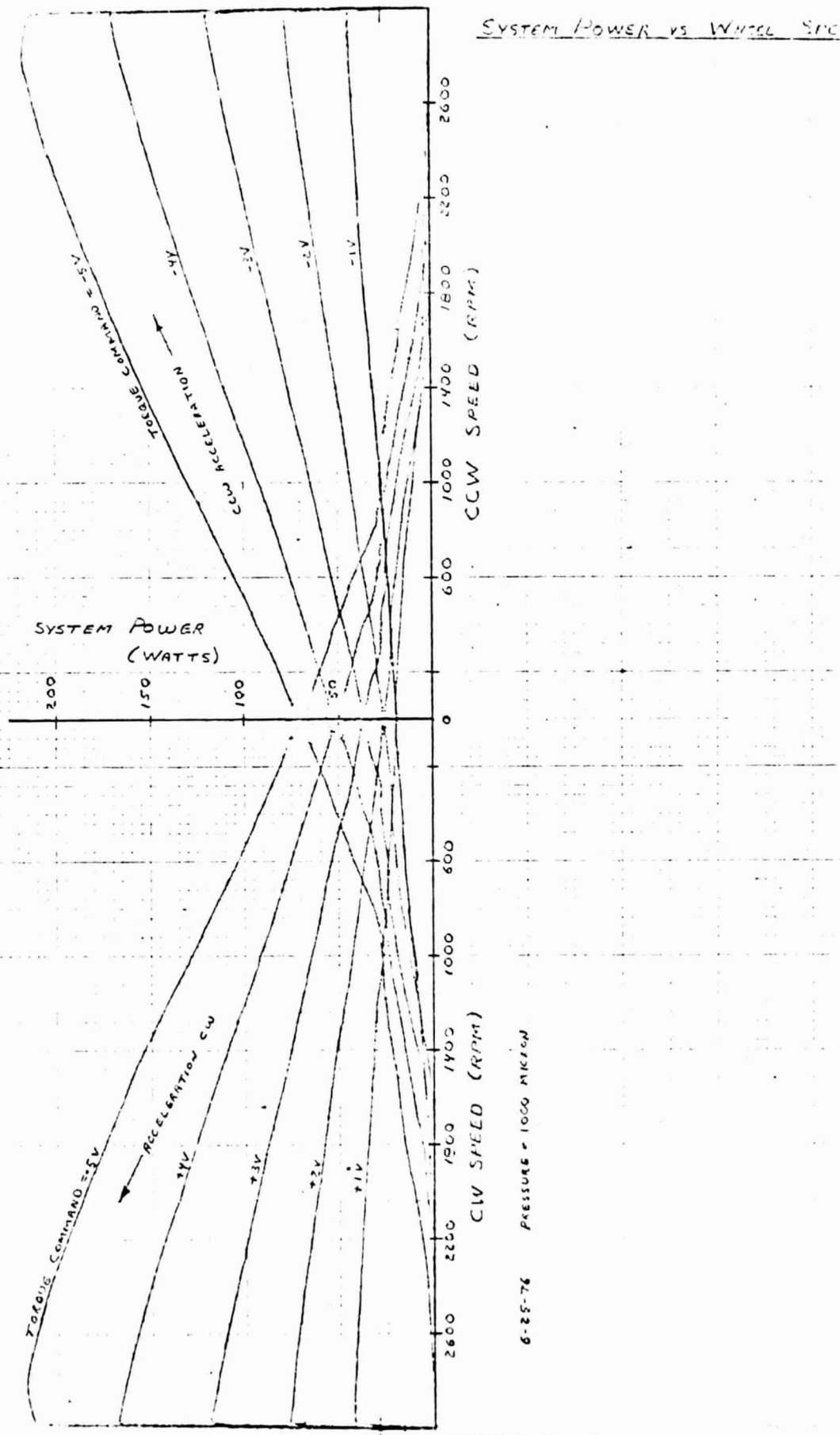
SYSTEM POWER VS WHEEL SPEED
SYSTEM POWER (WATTS)
200
150
100
50
0
CCW SPEED (RPM)
600
1000
1400
1800
2200
2600
TORQUE COMMAND = -5V
CCW ACCELERATION
-4V
-3V
-2V
-1V
CW SPEED (RPM)
TORQUE COMMAND = +5V
ACCELERATION CW
+4V
+3V
+2V
+1V
6-25-76 PRESSURE = 1000 MICRON

FIGURE 5-12

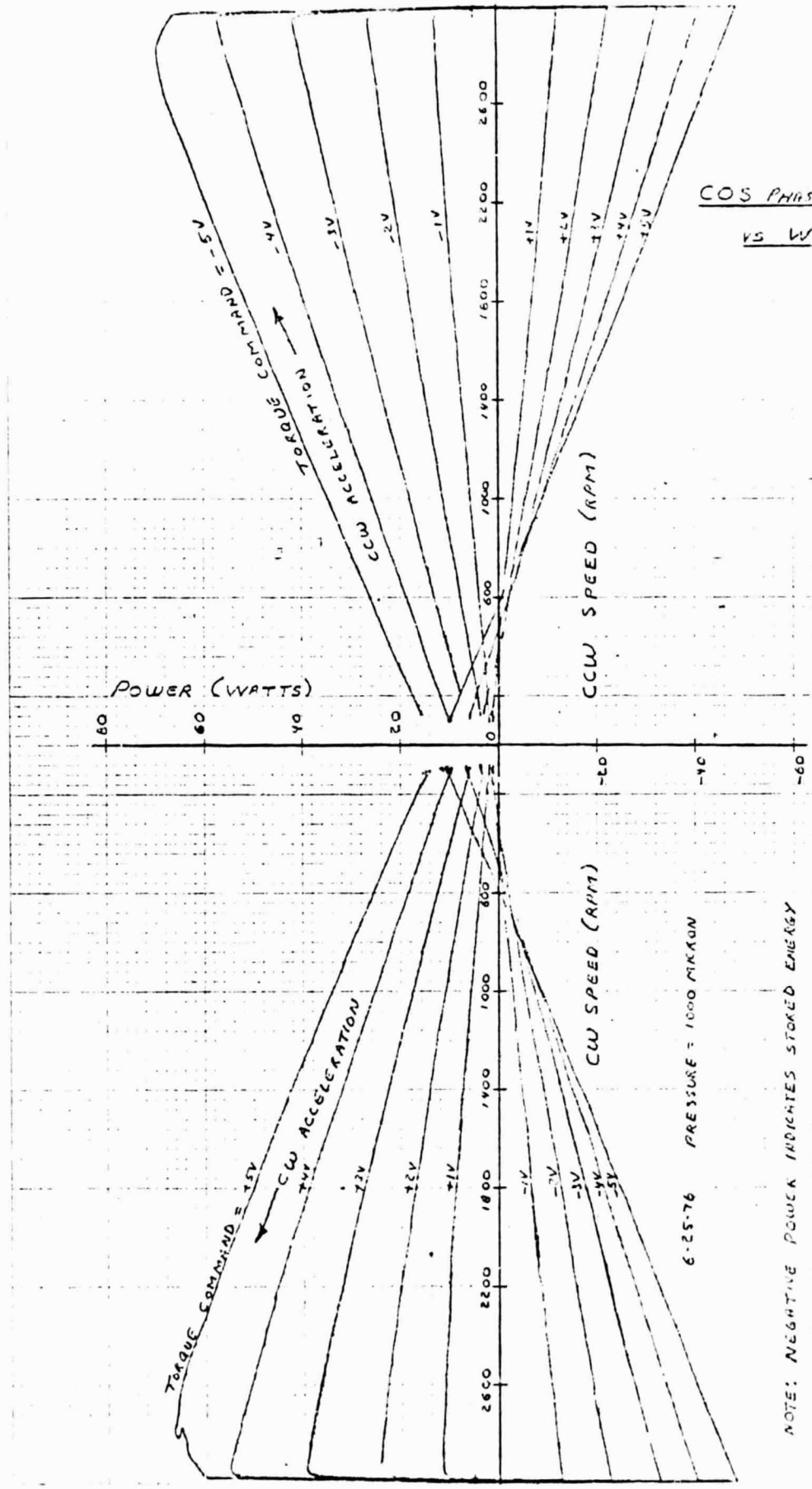

FIGURE 5-13
5-36

ORIGINAL PAGE IS
OF POOR QUALITY

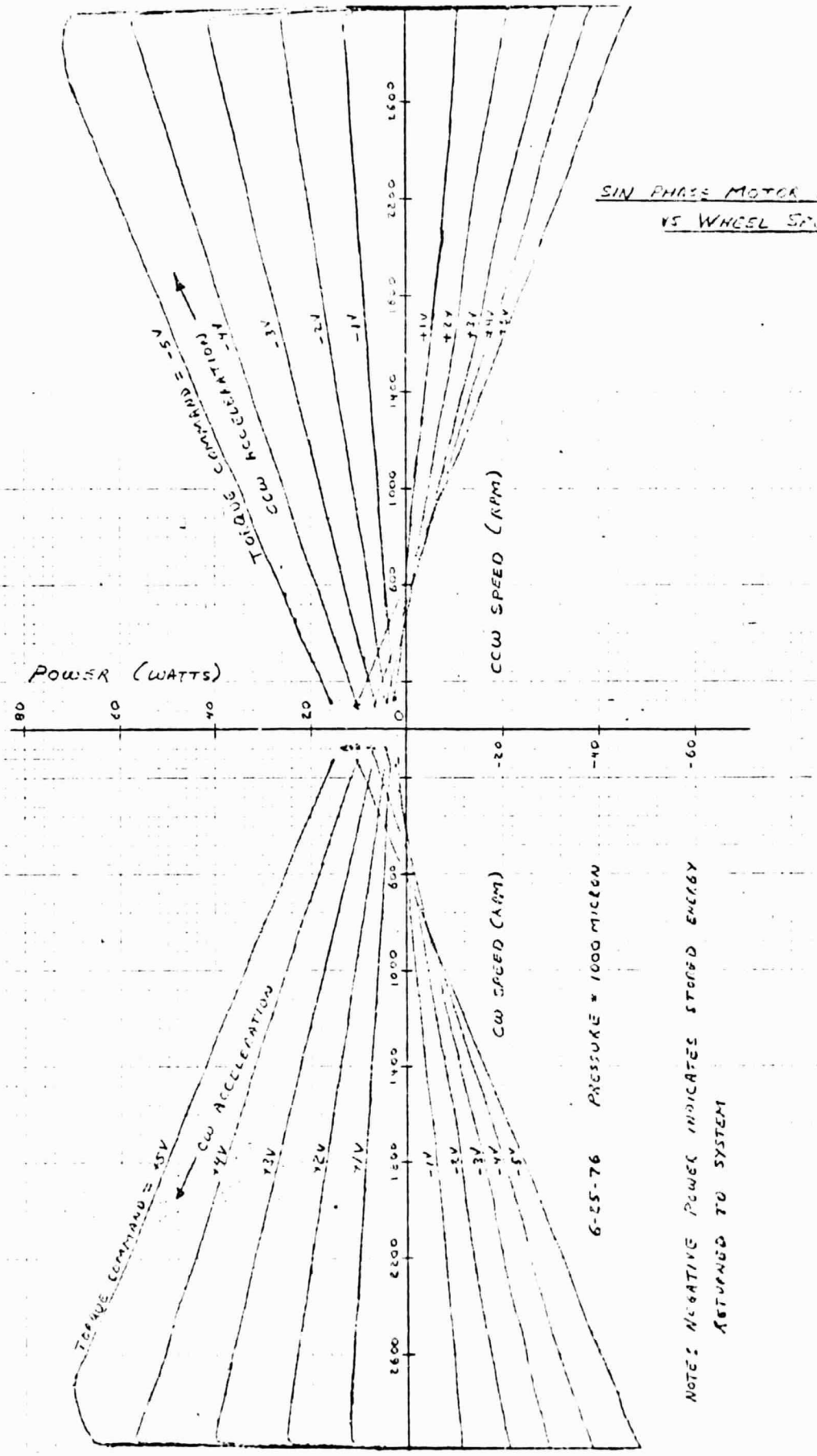
SIN PHASE MOTOR POWER
VS WHEEL SPEED
TORQUE COMMAND = -5V
CCW ACCELERATION
-5V
-3V
-2V
-1V
+1V
+2V
+3V
+4V
+5V
POWER (WATTS)
80
60
40
20
0
CCW SPEED (RPM)
600
1000
1400
1800
2200
2600
-20
-40
-60
TORQUE COMMAND = +5V
CW ACCELERATION
+5V
+4V
+3V
+2V
+1V
-1V
-2V
-3V
-4V
-5V
CW SPEED (RPM)
6-25-76
PRESSURE * 1000 MICRON
NOTE: NEGATIVE POWER INDICATES STORED ENERGY
RETURNED TO SYSTEM

FIGURE 5-14

50 FPS RW IRONLESS STATOR DC MOTOR

EFFICIENCIES VS SPEED AND TORQUE COMMAND

SPEED	0.	200.	400.	600.	800.	1000.	1200.	1400.	1600.	1800.	2000.	2200.	2400.
MOTOR													
TC													
1	0.0	32.0	47.7	62.6	68.3	71.4	79.9	72.6	85.5	85.4	88.7	91.1	92.2
2	0.0	39.2	55.5	65.0	73.2	79.2	81.0	81.2	86.8	88.2	90.9	91.5	93.8
3	0.0	32.4	50.4	60.3	67.5	71.9	76.1	78.9	81.4	83.7	84.8	85.8	86.1
4	0.0	28.9	45.1	55.2	62.5	67.8	72.1	75.0	78.1	79.8	82.1	83.6	86.3
5	0.0	24.9	39.7	49.7	57.0	63.3	67.5	71.2	73.8	76.7	78.7	81.4	81.2
ELECTRONICS													
TC													
1	17.5	26.2	33.0	34.4	40.0	44.8	44.1	54.8	48.5	50.7	52.0	53.2	55.0
2	23.1	29.2	38.3	43.7	46.9	50.0	60.1	57.8	57.3	60.3	60.9	58.4	54.4
3	28.4	37.5	47.6	47.2	51.3	55.0	57.9	59.9	61.6	62.8	64.8	65.6	67.1
4	31.7	39.6	45.5	50.0	53.0	55.4	57.5	58.6	59.7	61.5	62.2	62.2	62.9
5	36.4	42.6	46.8	50.0	52.1	53.1	54.6	55.7	57.1	58.1	58.5	60.6	62.0
H BRIDGE													
TC													
1	30.4	44.0	53.7	53.2	60.6	64.9	61.9	75.6	65.3	67.0	67.8	68.3	69.8
2	34.3	40.7	52.1	57.3	59.5	62.2	75.4	69.4	67.7	70.7	70.6	66.6	61.0
3	36.8	47.0	59.6	56.0	59.8	63.3	65.9	67.4	68.7	69.5	71.3	71.7	73.1
4	37.9	46.1	52.1	56.4	59.0	61.1	62.8	63.5	64.3	65.9	66.4	66.1	66.6
5	41.5	47.6	51.5	54.4	56.2	56.8	58.1	58.9	60.2	61.1	62.3	63.4	64.7
SUBSYSTEM													
TC													
1	0.0	8.3	15.7	21.5	27.3	31.7	35.2	39.2	41.4	43.3	46.2	48.5	50.6
2	0.0	11.4	21.2	28.4	34.3	39.6	48.7	46.9	49.7	53.2	55.3	53.5	51.0
3	0.0	12.2	24.0	28.4	34.6	39.5	44.0	47.2	50.1	52.6	54.9	56.3	57.7
4	0.0	11.4	20.5	27.6	33.1	37.6	41.5	44.0	46.6	49.0	51.1	52.0	54.3
5	0.0	10.6	18.6	24.8	29.7	33.6	36.8	39.7	42.1	44.6	46.8	49.4	50.4

TABLE 5-2

C.2

50 FPS RW IRONLESS STATOR DC MOTOR

MOTOR TORQUE SCALE FACTOR AND DRAG TORQUE VS SPEED

CC ACC

SPEED RPM	BIAS OZ*IN	S.F. OZ*IN/V
0.	-0.29	11.69
200.	-0.78	11.68
400.	-1.27	11.65
600.	-1.71	11.71
800.	-2.27	11.81
1000.	-2.87	11.93
1200.	-3.22	11.92
1400.	-3.65	11.95
1600.	-3.84	11.92
1800.	-4.27	11.99
2000.	-4.30	11.94
2200.	-4.51	11.91
2400.	-4.47	11.75
INTERCEPT	-0.66	AVG 11.835
SLOPE	-0.001853	SD 0.118
CORR	-0.977	

CW DEC

SPEED RPM	BIAS OZ*IN	S.F. OZ*IN/V
0.	0.26	11.68
200.	1.05	11.67
400.	1.36	11.66
600.	1.71	11.65
800.	2.73	11.61
1000.	2.35	11.63
1200.	2.69	11.63
1400.	2.80	11.66
1600.	3.00	11.62
1800.	3.34	11.56
2000.	3.41	11.57
2200.	4.04	11.42
2400.	4.36	11.36
INTERCEPT	0.78	AVG 11.594
SLOPE	0.001473	SD 0.094
CORR	0.969	

CW ACC

SPEED RPM	BIAS OZ*IN	S.F. OZ*IN/V
0.	0.98	-11.74
200.	1.30	-11.64
400.	2.31	-11.73
600.	2.46	-11.76
800.	2.62	-11.90
1000.	2.80	-11.66
1200.	3.19	-11.69
1400.	3.33	-11.67
1600.	3.77	-11.71
1800.	3.83	-11.59
2000.	4.21	-11.61
2200.	5.03	-11.89
2400.	4.81	-11.61
INTERCEPT	1.21	AVG -11.692
SLOPE	0.001576	SD 0.077
CORR	0.987	

CC DEC

SPEED RPM	BIAS OZ*IN	S.F. OZ*IN/V
0.	0.35	-11.71
200.	-0.29	-11.67
400.	-0.67	-11.71
600.	-1.62	-11.54
800.	-1.84	-11.58
1000.	-2.32	-11.48
1200.	-2.57	-11.49
1400.	-3.05	-11.41
1600.	-3.10	-11.44
1800.	-3.30	-11.42
2000.	-3.29	-11.45
2200.	-3.62	-11.40
2400.	-4.09	-11.29
INTERCEPT	-0.22	AVG -11.507
SLOPE	-0.001705	SD 0.128
CORR	-0.968	

TABLE 5-3

50 FPS RW IRONLESS STATOR DC MOTOR
MOTOR POWER VS SPEED AND TORQUE COMMAND

QUAD 1 CC ACC

SPEED	0.	200.	400.	600.	800.	1000.	1200.	1400.	1600.	1800.	2000.	2200.	2400.
TC													
1	3.5	5.0	7.0	8.0	10.0	12.0	13.0	19.0	16.0	18.0	19.5	21.0	23.0
2	6.0	8.5	12.5	16.0	19.0	22.0	25.5	31.0	32.0	35.5	38.5	41.5	44.5
3	10.5	16.0	20.5	26.0	31.0	36.0	41.0	46.5	51.5	56.0	61.0	66.5	74.5
4	16.5	24.0	31.0	38.0	44.5	51.5	58.0	65.0	71.5	78.5	84.5	91.5	97.5
5	25.5	35.5	44.0	52.5	61.5	69.5	78.5	86.5	95.5	103.5	111.5	119.5	128.0

QUAD 2 CW DEC

SPEED	0.	200.	400.	600.	800.	1000.	1200.	1400.	1600.	1800.	2000.	2200.	2400.
TC													
1	3.5	2.5	0.5	-0.5	-3.0	-5.0	-7.0	-9.0	-11.0	-13.0	-15.5	-16.5	-19.0
2	6.0	2.5	0.5	-3.5	-7.0	-10.0	-13.5	-17.0	-20.5	-24.0	-26.5	-30.0	-33.5
3	10.5	5.0	0.5	-4.0	-9.5	-14.0	-18.5	-23.5	-29.0	-34.0	-38.0	-42.5	-47.0
4	16.5	9.5	3.5	-3.5	-9.5	-16.0	-22.5	-29.0	-35.0	-41.5	-48.0	-54.0	-59.5
5	25.5	17.0	8.0	-0.5	-9.0	-16.5	-25.0	-33.0	-40.5	-48.5	-57.0	-64.5	-72.5

QUAD 3 CW ACC

SPEED	0.	200.	400.	600.	800.	1000.	1200.	1400.	1600.	1800.	2000.	2200.	2400.
TC													
1	3.5	6.0	7.5	8.5	10.0	12.0	13.0	15.0	16.0	17.5	18.5	20.0	21.0
2	6.0	9.0	12.0	15.5	18.5	21.5	25.0	28.0	31.0	34.5	37.0	40.0	41.5
3	10.5	15.5	20.0	25.0	30.0	35.5	40.0	44.5	49.5	54.5	59.5	64.0	66.5
4	16.5	23.5	30.0	37.0	44.0	50.5	57.0	64.0	70.5	77.0	83.5	89.5	93.0
5	25.5	34.0	43.0	52.0	60.0	68.0	76.5	85.0	93.0	100.0	108.5	117.0	125.5

QUAD 4 CC DEC

SPEED	0.	200.	400.	600.	800.	1000.	1200.	1400.	1600.	1800.	2000.	2200.	2400.
TC													
1	3.5	2.5	0.5	-0.5	-2.5	-5.0	-7.0	-9.0	-11.0	-13.0	-15.0	-16.5	-18.5
2	6.0	2.5	0.5	-4.0	-7.0	-10.0	-14.0	-17.5	-21.0	-24.5	-26.5	-30.0	-33.0
3	10.5	5.0	0.5	-4.0	-10.0	-14.0	-19.5	-25.0	-30.0	-34.5	-38.0	-43.5	-49.0
4	16.5	9.0	3.0	-4.0	-10.0	-17.0	-22.5	-30.0	-35.5	-42.5	-49.0	-55.0	-60.5
5	25.5	16.0	8.5	-0.5	-8.5	-17.0	-25.0	-33.5	-41.5	-49.0	-57.0	-65.5	-74.0

REGRESSION LINES (POWER VS SPEED), (POWER/SPEED VS TORQUE COMMAND)

	QUAD 1 AND 2			QUAD 3 AND 4		
TC VOLT	SLOPE WATTS/KRPM	BIAS WATTS	CORR	SLOPE WATTS/KRPM	BIAS WATTS	CORR
1	8.67	3.15	0.9963	-8.39	2.90	-0.9964
2	16.35	6.00	0.9997	-15.91	5.50	-0.9996
3	25.00	11.27	0.9997	-24.24	10.42	-0.9999
4	33.19	17.81	0.9998	-32.68	17.19	-0.9998
5	42.27	26.73	0.9998	-41.58	25.83	-0.9999
TORQUE CONSTANT		8.40		-8.31	WATTS/KRPM/VOLT	
		11.36		-11.24	OZ*IN/VOLT	
		8.12		-8.03	OZ*IN/PEAK AMP	
BIAS		-0.11		0.39	WATTS/KRPM	
CORR		0.9996		-0.9996		
I SQR R CONSTANT		0.50		0.49	OHMS	
BIAS		2.19		1.81	WATTS	
CORR		0.9999		0.9999		

TABLE 5-4
5-40

ORIGINAL PAGE IS
OF POOR QUALITY

SECTION 6.0
CONCLUSIONS AND RECOMMENDATIONS

The feasibility of a magnetically suspended reaction wheel in the 50 to 100 ft-lb-sec class has been demonstrated. Although some of the goals set forth were not fully reached, the basic premise was accomplished, i.e., to magnetically suspend the 50 ft-lb-sec reaction wheel within its own envelope. Structural resonances have proven to be as important in the design as the magnetic suspension itself. The need for careful design and precision machining because of the large diameters and magnetic forces has been made clear. Therefore, although the basic concepts have been proven, much work remains to be done in refining the magnetic suspension into a practical bearing.

The work on this suspension concept should be continued in a two fold manner. The 50 ft-lb-sec MBSRW should continue to be worked on so as to learn as much as possible from a working model. A new ironless stator brushless DC motor, without circulating currents, should be installed to eliminate motor drag torques. Experience and knowledge can be gained in the areas of magnetic fields, displacement and velocity sensors, servo mechanisms and assembly techniques. A second concurrent effort should be started with the design of a new reaction wheel. This design should concentrate on the magnetic suspension and structure with the wheel being designed into the suspension rather than the suspension being designed around the wheel. In this manner many of the problems encountered during this experiment should be reduced.